Experimental simulation of chemomechanical processes during deep burial diagenesis of carbonate rocks

L. Neveux, D. Grgic, C. Carpentier, J. Pironon, L. Truche, J. P. Girard

AGU PUBLICATIONS

JGR

Journal of Geophysical Research: Solid Earth

RESEARCH ARTICLE
10.1002/2013JB010516

Key Points:
- A new experimental setup is designed to investigate deeply buried reservoirs
- The main process during carbonate deep diagenesis is pressure solution creep
- Influence of stress on calcite solubility is very significant

Correspondence to:
D. Grgic,
dragan.grgic@univ-lorraine.fr

Citation:
Neveux, L., D. Grgic, C. Carpentier, J. Pironon, L. Truche, and J. P. Girard (2014), Experimental simulation of chemomechanical processes during deep burial diagenesis of carbonate rocks, *J. Geophys. Res. Solid Earth*, *119*, 984–1007, doi:10.1002/2013JB010516.

Received 10 JUL 2013
Accepted 24 JAN 2014
Accepted article online 29 JAN 2014
Published online 25 FEB 2014

Experimental simulation of chemomechanical processes during deep burial diagenesis of carbonate rocks

L. Neveux[1], D. Grgic[1], C. Carpentier[1], J. Pironon[1], L. Truche[1], and J. P. Girard[2]

[1]GeoRessources Laboratory, BP 40, University of Lorraine/CNRS/CREGU, Vandoeuvre-lès-Nancy, France, [2]TOTAL CSTJFI, Pau, France

Abstract Chemomechanical processes involved in the deep burial diagenesis of carbonate petroleum reservoirs are still poorly understood. To better understand these processes and explain how porosity and permeability can be preserved at the great depth of DBRs (deeply buried reservoirs), we developed an experimental device allowing both the simulation of high-pressure/stresses/temperature conditions (80°C, 60 MPa of confining pressure, and differential stress up to 40 MPa) of DBR and the circulation of different fluids in rock samples. We tested (triaxial multistep creep tests) four core samples of a cemented limestone and analyzed creep deformations, fluids chemistry, and petrographical and petrophysical properties of samples. Different flow conditions (no flow and flow through) and chemical compositions (natural meteoric water with and without phosphate ions) were considered. Our study showed that the precipitation of calcite on free pore walls of micrites blocks the microporosity between micrite crystals, thus rendering the microporosity inaccessible to fluids. Hence, the connected porosity decreased strongly after experimentation. This is due to the PSC (pressure solution creep) which is the main process implied in the porosity reduction of a carbonate rock during deep burial. The preservation of macropores during PSC allows the preservation of permeability. In addition, calcite solubility is positively dependent on mechanical parameters (axial compaction and axial stress), thus suggesting that calcite can precipitate during decompression of deep basinal fluids, resulting in changes in porosity. A comparison of experimental results with theoretical calculations showed that the integration of the PSC process into calculation databases would greatly improve the modeling of DBR.

1. Introduction

The abundance of hydrocarbons in so-called conventional reservoirs is rapidly declining as the demand for energy is continually increasing. Oil and gas production are being pushed to new limits. In this context, the study of unconventional petroleum reservoirs is of great interest. Deeply buried reservoirs (DBRs) are high-quality reservoirs buried more than 4000 m deep: they are a type of unconventional reservoir that has been historically overlooked. The main properties of hydrocarbon reservoirs are high porosity and permeability. However, conventional modeling of carbonate evolution during burial shows a decrease in porosity and permeability with depth and a nearly complete absence of reservoir qualities below 4000 m [e.g., *Friedman et al.*, 1981; *Schmoker and Halley*, 1982; *Schmoker*, 1984; *Ehrenberg and Nadeau*, 2005]. Thus, the discovery of DBR raises an important question: how might porosity and permeability be preserved at great depth?

Under the stresses/temperature conditions of DBR, many deformation mechanisms may be involved in the material compaction. These include cataclastic flow (i.e., grain crushing) [*Zhu et al.*, 2010], subcritical crack growth [*Atkinson*, 1984; *Atkinson and Meredith*, 1987; *Lockner*, 1993; *Røyne et al.*, 2011; *Brantut et al.*, 2013], and intergranular pressure solution resulting in pressure solution creep (PSC) [*Gratier*, 1993; *Weyl*, 1959; *Zubtsov et al.*, 2004; *Croizé et al.*, 2010a, 2013]. Intergranular pressure solution is considered by many authors [e.g., *Lehner*, 1995; *Rutter*, 1983; *Tada and Siever*, 1989; *Leythaeuser et al.*, 1995] to be the main mechanism responsible for the decrease in petrophysical properties (porosity and permeability) at great depth. This chemomechanical process, which is very important in the case of carbonate rocks, involves dissolution of solids and removal of the dissolved material by the way of pore fluids.

Although numerous studies [e.g., *Friedman et al.*, 1981; *Schmoker and Halley*, 1982; *Ehrenberg and Nadeau*, 2005; *Baud et al.*, 2009; *Coelho et al.*, 2006; *Croizé et al.*, 2010b; *Xie et al.*, 2011; *Dautriat et al.*, 2011] have shed a great deal of light on carbonate diagenesis, a complete picture of burial processes still eludes us. Indeed,

conventional methods of study for burial diagenesis usually involve petrographical observations focused on a particular geological target. However, a general understanding of the processes involved in the burial diagenesis of carbonate rocks is needed. The majority of recent experimental work on carbonates has focused on either mechanical processes or fluid-rock interactions alone. Most studies conducted under high pressure were performed under dry conditions [*Baud et al*., 2009; *Vajdova et al*., 2012] and focused on the mechanical behavior of rock material [*Coelho et al*., 2006; *Croizé et al*., 2010a; *Xie et al*., 2011; *Wong and Baud*, 2012], thus neglecting fluid effects in diagenesis simulation. Conversely, studies focusing on fluid-rock interactions were conducted under conditions not representative of DBR [*Price et al*., 2010; *Jonasson et al*., 1996; *Meyer*, 1984; *Zhang and Spiers*, 2005a], thus neglecting the effect of pressure/stresses. Therefore, an innovative method for the experimental simulation of chemomechanical conditions in deep reservoirs was developed for the purpose of this study. This new multidisciplinary approach has the potential to generate interest because of how it couples the mechanical conditions of DBR (high fluid pressure, stresses, and temperature) with fluid-rock interactions. Indeed, as emphasized by *Bjørlykke and Høeg* [1997], the integration of parameters such as temperature, pressure/stresses, and fluid-rock interactions is required to better understand diagenetic processes in deeply buried environments.

To better understand chemomechanical processes involved in the deep burial diagenesis of carbonate petroleum reservoirs and explain how porosity and permeability can be preserved at the great depth of DBRs (deeply buried reservoirs), we developed an experimental device allowing both the simulation of high-pressure/stresses/temperature conditions of DBR and the circulation of different fluids in carbonate samples. For the purpose of our multidisciplinary study, four core samples are tested mechanically (triaxial multistep creep tests) and creep deformations, chemistry of pore fluids, and petrographical and petrophysical properties of samples are analyzed. As most carbonates are already strongly cemented at subsurface depths ($<$1000 m) [*Croizé et al*., 2010b], experimentation on weakly cemented samples avoids the impacts of diagenesis and allows the observation of the effects of our artificial burial. Since the chemical composition of a percolating fluid within a carbonate rock has a great influence on the processes of dissolution and precipitation, thus affecting reservoir quality, we tested fluids with different flow conditions (no flow and flow through) and chemical compositions (natural meteoric water and natural meteoric water enriched in phosphates). Natural meteoric water was used in our experiments to simulate the circulation of meteoric water in a reservoir formation. Phosphate is an important constituent of sea and pore waters, interacting with carbonate rocks during burial diagenesis. In addition, inhibiting effects of phosphate ions on intergranular pressure solution in calcite is well described in specialized literature in this field [e.g., *Zhang and Spiers*, 2005b].

2. Experimental and Modeling Methods: A New Multidisciplinary Approach

2.1. Chemomineralogical and Petrophysical Description of the Initial Rock

Chemomechanical experiments were performed on an early cemented bioclastic limestone (Bathonian, Middle Jurassic) whose calcite percentage is about 98. This limestone is composed of ooids, pellets, and bioclasts (brachiopods, echinoderms, foraminifers, gastropods, and bivalves), as shown in Figure 1 which represents thin section images of Massangis limestone impregnated with blue resin in its natural state. The rock matrix is micritic (Figure 1), and some early spar cements can be observed. The limestone is highly (macro) porous on the Figure 1 (left), whereas Figure 1 (bottom right) shows a very micritic zone without macropores, thus illustrating the high heterogeneities of the rock. The micrite is microporous and permeable, allowing for the flow of fluids, whereas the sparite crystals are blocky and impermeable. The limestone was sampled in the active quarry of Massangis (Burgundy, France). All analyses were performed on the same cored borehole. The cylindrical samples used for the mechanical experiments were cored in the direction perpendicular to the horizontal sedimentary bedding of the rock. The chemical composition of the limestone, analyzed by ICP-ES (inductively coupled plasma-emission spectrometry), is described in Table 1. This particular limestone outcrop was selected because it represents a surface analog of DBR and is therefore a good initial sample for studying the effects of burial diagenesis.

The porosity of the initial Massangis limestone was analyzed via different porosimetry techniques (Table 2). The total porosity n_t, which includes both connected (i.e., open) and not connected (i.e., closed) porosities, was measured using helium pycnometer ($n_t = 1 - \rho_d/\rho_s$, ρ_d is the density of the dry rock, and ρ_s is the density of the rock skeleton). Water-connected porosity n_w was also determined by immersion in water. Since

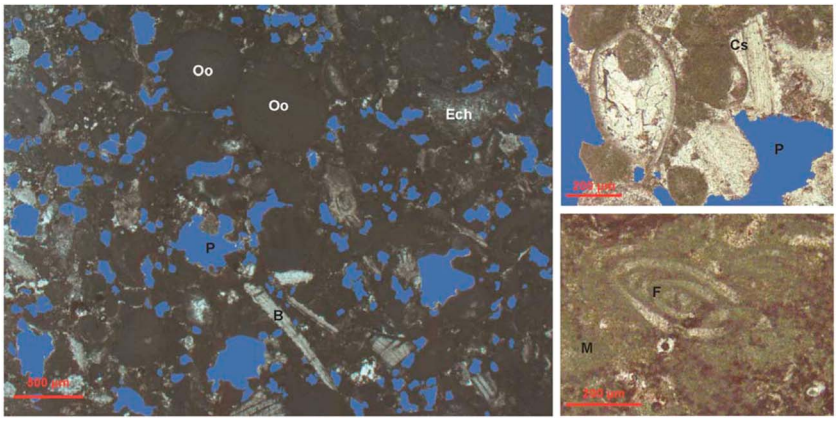

Figure 1. Thin section images of initial (i.e., before experimentation) Massangis limestone impregnated with blue resin in its natural state. These images show the rock's heterogeneity, porosity (*P*), and major components: (Oo) Ooïds, (Ech) Echinoderm fragments, (B) Bivalve, (F) Foraminifera, (Cs) syntaxial cement, and (M) micritic matrix.

water-connected porosity n_w (~ 19.6%) is almost equal to the total porosity n_t (~ 19.4%), porosity can be considered as entirely connected/open, i.e., there are no closed pores in grains. The porosity of the initial Massangis limestone was also analyzed via two Purcell tests (mercury intrusion porosimetry) on rock cuttings taken very close to the mechanically tested core samples. This test allows the determination of the porous spectrum (i.e., distribution of entrance radii of pores) and the (total/bulk) mercury connected porosity which includes both free and trapped porosities. Results of this test are also presented in Table 2. Figure 2a shows a porous spectrum obtained on a sample from the first mercury injection with a mercury pressure up to 400 MPa. This spectrum shows a widespread (i.e., poorly sorted) and multimodal (with a slight bimodal tendency) distribution of pore throat size and is composed of pores of entrance radii between 0.01 μm and 50 μm in size. Table 2 shows that the free porosity (5.9%) represents a small fraction of the total porosity (18.6%) which is consistent with the widespread distribution of the porous spectrum. The large fraction of trapped porosity (12.7%) corresponds to large pores with limited pore accessibility. This results in a relatively high water permeability of 25 mdarcy (= 2.5×10^{-14} m^2). Moreover, since water saturation porosity (19.6%), which is the best technique for the determination of the connected porosity (because of the high wetting properties of water), is very close to the total mercury porosity (18.6%), this signifies that mercury intrusion porosimetry is an appropriate technique for the characterization of the connected porosity of the Massangis limestone. Besides, the good petrophysical properties of Massangis limestone (porosity of 18.6% and intrinsic water permeability of 25 mdarcy) enable a steady flow of fluids during experimentations and relatively short test duration (cf. Table 2). Actually, the Massangis limestone is a rock with significant natural heterogeneities and we chose the most permeable and porous facies (in the active quarry of Massangis, Burgundy, France) to facilitate our experiments.

Table 1. Chemical Composition of Massangis Limestone[b]

Oxides	Weight Percent
SiO_2	< 0.5
Al_2O_3	0.09 [a]
Fe_2O_3	0.35 ± 0.02
MnO	0.0044 [a]
MgO	0.41 ± 0.04
CaO	54.27
Na_2O	< 0.03
K_2O	0.03 [a]
TiO_2	0.005 [a]
P_2O_5	< 0.05
Loss on ignition	43.4
Total	98.56

[a]For Al_2O_3, MnO, K_2O and TiO_2, uncertainty is > 25%.
[b]Elements were analyzed by ICP-ES.

2.2. Description of the Experimental Device

To simulate the in situ conditions of deeply buried reservoirs (DBRs), a new experimental device was designed (Figure 3). This device allows for the recording of hydromechanical parameters (stresses, fluid pressure, and strains) and sampling of percolating fluid during the mechanical tests. It has been designed to simulate fluid injection and/or saturation under the pressure/stresses/temperature conditions of deep reservoirs: confining pressures and differential stresses up to 100 MPa, fluids pressures up to 60 MPa, and temperature up to 150°C. Different kinds of fluid, such as water, brine, or oil, can be injected into the tested samples. The setup consists of three main components: the triaxial cell

Table 2. Porosity Measurements on Massangis Limestone: Initial Sample and Samples After Experiments I, II, III, and IV

	Mercury Connected Porosity (%) (Two Measurements)			Density of Solid Matrix	Density of the Dry Rock	Total Porosity (%)
Sample	Total	Free	Trapped	ρ_s (g/cm^3)[a]	ρ_d (g/cm^3)	$n_t = 1 - \rho_d/\rho_s$
Initial	18.6 ± 1.2	5.9 ± 1.1	12.7 ± 2.2	2.69	2.17	19.4
Experiment I	16.9 ± 1.6	5.7 ± 0.2	11.2 ± 1.6	2.73	2.18	20.3
Experiment II	6.5 ± 1.3	1.7 ± 0.9	4.8 ± 1.2	2.78	2.15	22.7
Experiment III	8.8 ± 3.2	2.5 ± 1.2	6.3 ± 2.1	2.79	2.16	22.8
Experiment IV	17.0 ± 0.2	6.4 ± 0.1	10.6 ± 0.1	2.71	2.15	20.7

[a]Measurements of the rock skeleton (matrix) density were conducted by helium pycnometer.

and loading system (Figures 3a and 3b), the system for fluid circulation (Figure 3c), and the control station and data acquisition system (Figures 3d and 3e).

The autonomous and self-compensated triaxial cell allows confining pressure ($Pc = \sigma_{11} = \sigma_{22} = \sigma_{33}$) and differential stress q to be applied separately. This configuration facilitates tests under different loading paths, including isotropic (i.e., hydrostatic) and deviatoric. Under axisymmetric compression on cylindrical samples, the von Mises equivalent stress (i.e., the differential stress) is

$$q = \sigma_{eq} = |\sigma_{11} - \sigma_{33}| \quad (1)$$

The convention of positive compressions for stresses and strains was used in this study (σ_{11} is the axial stress, and σ_{33} is the lateral stress).

The triaxial cell (Figure 3a) is heated by three metal collars, which are controlled by an independent heating unit. The triaxial cell includes many inlets/outlets that allow for the injection/extraction of fluids (cf. Figure 3). Fluids pressures are controlled by pressure generators (syringe pumps, 100 mL capacity) which are equipped with temperature control jackets. Pressure generators can apply a constant flow of fluid (range: 0.00001–30 mL/min) or a constant fluid pressure. Confining pressure Pc and axial stress σ_1 are applied through oil pressure (Figure 3b). The injection/extraction of different kinds of fluids (water, brine, hydrocarbons, and gaz) is allowed by pressure generators that are connected to the inlet/outlet of the triaxial cell (Figure 3c), thus generating interstitial pressure Pi into the tested sample. Valves, which are connected between pressure generators and the triaxial cell, allow for the sampling of the interstitial

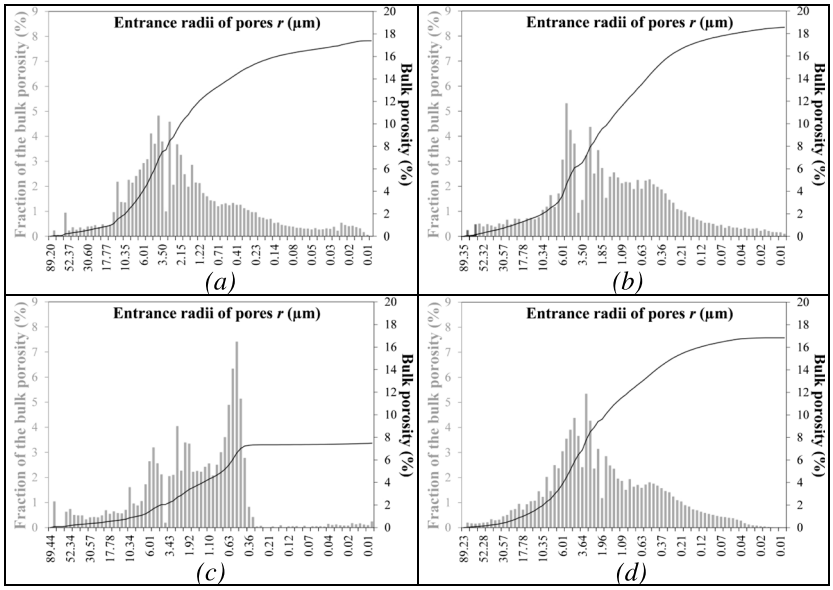

Figure 2. Characteristic porous spectra (distribution of entrance radii of pores for bulk porosity, first injection of Hg porosimetry) of Massangis limestone. (a) Initial sample. (b) Sample after Experiment I (closed and no-flow condition). (c) Sample after Experiment II (dynamic percolation of the meteoric water). (d) Sample after Experiment IV (dynamic percolation of the meteoric water enriched in phosphates).

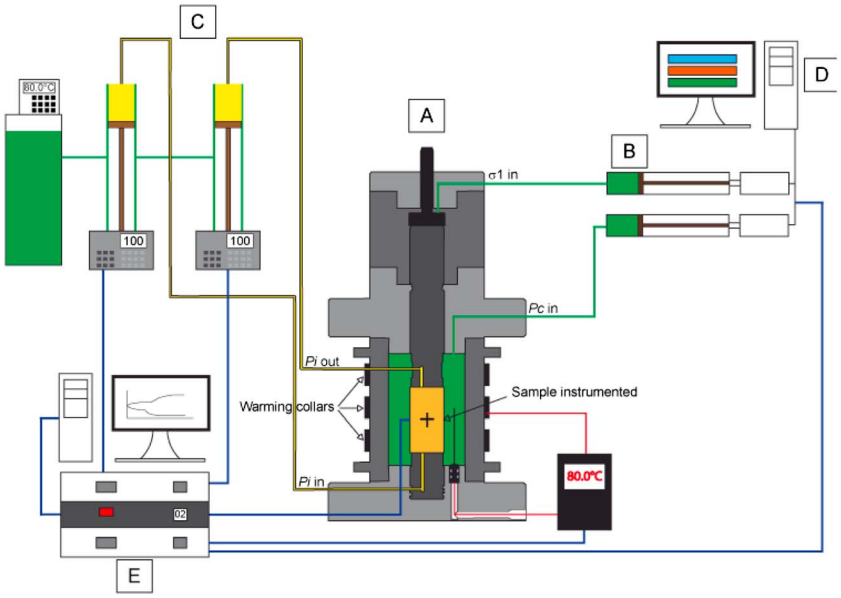

Figure 3. Schematic representation of the high-pressure triaxial setup (σ_1: axial stress, Pc: confining pressure, and Pi: interstitial pressure). (a) Triaxial cell. (b) Loading unit. (c) Fluid circulating system. (d) Control station. (e) Data acquisition system.

fluid. To ensure a uniform distribution of the percolating fluid in the cylindrical sample, two uniformly perforated metal disks (with a thickness of 5 mm) are placed between cylindrical seats and sample (injection point at the bottom plate and extraction point at the loading piston). The control station and the data acquisition system (Figures 3d and 3e) allow for the independent regulation of experimental parameters (fluid pressures and temperature) and the recording of experimental data (strains, axial stress, confining stress, interstitial fluid pressure, temperature, and injected volumes of interstitial fluid). The sampling frequency for data acquisition was 1 min for the multistep creep tests and 10 s for the short-term triaxial compression tests.

We tested cylindrical samples of Massangis limestone of 38 mm in diameter and 76 mm in height. Sample deformation was measured with six strain gauges: three axial and three circumferential (i.e., lateral), as shown in Figure 4. The core sample is jacketed by a 5 mm thick Viton sleeve (Figure 4) to prevent the hydraulic fluid (i.e., oil) from penetrating the rock specimen and the interstitial fluid from escaping outside the core sample.

2.3. Experimental Procedure

Four long-term experiments were performed to determine the effects of fluid circulation on petrophysical properties during burial diagenesis. We choose the stress-stepping technique for the mechanical loading under triaxial conditions (i.e., triaxial multistep creep tests). There are a lot of benefits to perform stress-stepping experiments; it saves a lot of laboratory time and can be used to apply any loads, thus providing a large amount of data from a single sample without being confronted with the issue of repeatability. All experiments were performed at pressure/stresses/temperature conditions representative of DBR. Because the focus of our study was not to reproduce a specific reservoir, mean values for vertical and horizontal stresses were selected. It is usually assumed that vertical stress is the primary stress in sedimentary basins [*Holbrook*, 1999]. The maximum vertical stress σ_v used in the experiments ($\sigma_v = \sigma_{11}$ max = 100 MPa = Pc + q max) corresponds to a mean burial of 4500 m in DBR such as the central North Sea [*Holbrook*, 1999], Aquitaine basin [*Bell and Caillet*, 1994], St. Lawrence Lowlands basin [*Konstantinovskaya et al.*, 2012], and Cuu Long basin [*Binh et al.*, 2007]. We also assumed isotropic horizontal stresses (i.e., $\sigma_h = \sigma_{22} = \sigma_{33}$) and that both horizontal stresses are lower than the vertical stress (i.e., $\sigma_h < \sigma_v$). The horizontal stress for our experiments was σ_h = Pc = 60 MPa and is a mean value corresponding to values reported by *Binh et al.* [2007] and *Bell and Caillet* [1994]. The interstitial pressure was Pi = 30 MPa which is also a mean reservoir value. This results in an effective confining pressure (Pc′ ~ Pc−Pi) of 30 MPa. All experiments were performed at T = 80 ± 1°C which is representative of a depth of 4500 m by considering a small thermal gradient.

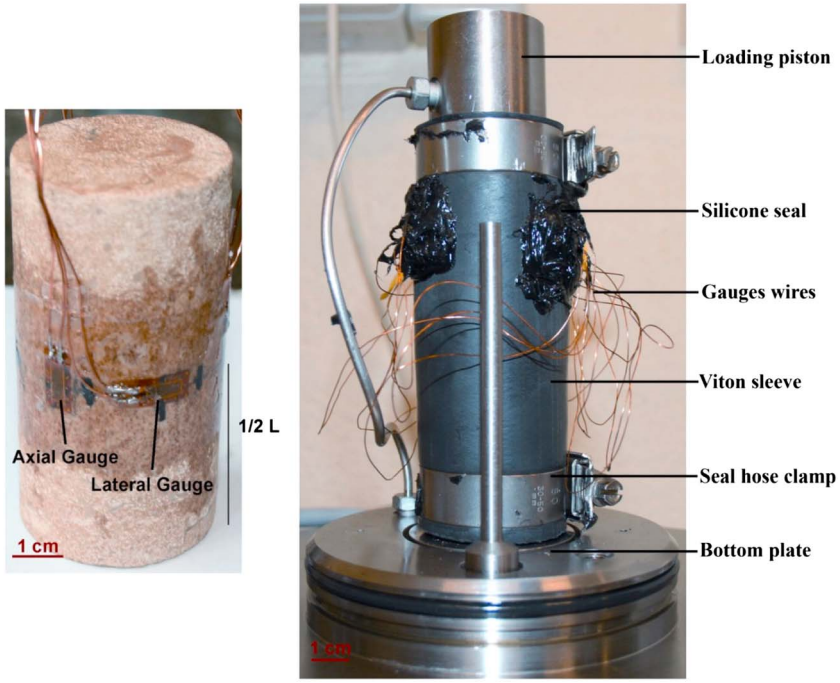

Figure 4. Cylindrical core sample of Massangis limestone, instrumented with strain gauges and set up between the cylindrical seats (i.e., loading piston at the top and bottom plate) of the triaxial cell.

A natural meteoric water (salinity < 0.2 g/L) was used in our experiments as the interstitial fluid. The chemical composition and *pH* of this initial fluid is given in Table 3. The solution was allowed to equilibrate with atmospheric CO_2 at 20°C before reacting with the core sample at 80°C. All core samples were saturated with this solution. In the Experiment I, we considered closed and no-flow condition (i.e., no fluid circulation). Experiments II and III were performed with a dynamic percolation and continuous renewal of the meteoric fluid (i.e., open circuit or flow-through condition). To analyze the influence of the loading path, the sample was loaded with four stress increments in the Experiment II and with two stress increments in the Experiment III. In the Experiment IV, the meteoric fluid was enriched in phosphates (NaH_2PO_4) and a dynamic percolation with continuous renewal was considered. In this experiment, the phosphate's concentration was 10^{-3} mol/L.

Table 3. Ionic Composition and pH of the Initial (Input) Fluid, the Interstitial Fluid After the Experiment I (Closed and No-Flow Condition), and the Output Fluid During Experiment II (Dynamic Percolation of the Meteoric Water With Four Stress Increments)

	Creep Time (days)	Differential Stress q (MPa)	pH	$[Ca^{2+}]$ (mg/L)	$[Mg^{2+}]$ (mg/L)	$[Fe_{tot}]$ (mg/L)	$[CO_3^{2-}]$ (mg/L)
Initial fluid	-	-	7.62	47	7.1	0.005	36.2
Interstitial fluid after Experiment I	-	0–40	6.92	151	2.7	0.09	49.8
Output fluid during Experiment II	2	0	7.90	59	5.2	0.008	-
	4	0	7.82	51	5.4	0.003	40.8
	9	10	7.76	93	16.6	0.006	-
	14	10	7.66	57	4.9	0.007	44.8
	18	20	7.80	112	1.2	0.012	-
	21	20	7.81	107	1.0	0.009	-
	24	20	7.73	101	1.1	0.022	46.8
	28	30	7.81	106	1.2	0.021	-
	32	30	7.77	141	0.9	0.022	-
	36	30	7.74	182	1.0	0.038	-
	39	30	7.72	237	2.1	0.039	50.6
	42	40	8.07	180	0.8	0.028	-
	45	40	7.80	187	0.5	0.047	-
	49	40	7.68	191	0.7	0.047	-
	51	40	7.76	219	0.6	0.050	-
	55	40	7.66	246	0.5	0.037	-
	58	40	7.81	243	0.5	0.039	53.4

This concentration was chosen because previous studies [e.g., *Zhang and Spiers*, 2005b] showed that it is the most efficient for inhibiting intergranular pressure solution in calcite. The experimental conditions were progressively applied in the following order for the triaxial multistep creep tests: (1) application of a low confining pressure (Pc = 1.5 MPa) for the sample saturation; (2) saturation of the sample with the natural meteoric water in the triaxial cell (Pi = 1 MPa); (3) increase of the temperature (T = 80°C); (4) application of the confining pressure (Pc = 60 MPa), hydrostatic loading rate = 0.25 MPa min^{-1}; (5) application of the interstitial pressure (Pi = 30 MPa), loading rate = 0.25 MPa min^{-1}; (6) beginning of the dynamic percolation of the interstitial fluid (for Experiments II and III) under hydrostatic loading during a few days; (6) incremental increase of the differential stress q (σ_{11} max = 100 MPa and q max = 40 MPa), loading rate = 0.25 MPa min^{-1}.

We also performed short-term uniaxial (Pi = 0 MPa and Pc = 0 MPa) and triaxial (Pi = 1 MPa and Pc = 7, 15, and 31 MPa) compression tests under drained condition to characterize the yield and strength properties of the Massangis limestone. Short-term compression tests were also performed at T = 80°C. Loadings of these short-term triaxial tests and loadings of the triaxial multistep creep tests were performed at the same rate (0.25 MPa min^{-1}). Sample deformation was measured with strain gauges, and the axial deformation was also measured with an external linear variable differential transformer (LVDT) sensor which allows the characterization of the postpeak behavior. It is worth emphasizing that the relatively high permeability of the tested rock (25 mdarcy = 2.5×10^{-14} m^2) allowed drained conditions (i.e., constant pore water pressure) during short-term triaxial compression tests and long-term triaxial multistep creep tests.

2.4. Methods of Analysis

2.4.1. Chemical Analyses of Fluids

During the Experiments II and III, the percolating fluid was sampled regularly (every 3 days) in a 2 mL hermetic container to measure variations in the fluid composition over time. The volume of the sampled fluid was 1 to 2 mL. pH was measured at room temperature with a combined pH probe. Because such a small quantity of fluid was sampled, LA-ICP-MS (laser ablation-inductively coupled plasma-mass spectrometry) was used for the chemical analysis of all solutions. LA-ICP-MS is a device available at GeoRessources Laboratory, which development by *Leisen et al*. [2012a, 2012b] enables the analysis of small quantity of fluid. The LA-ICP-MS system is composed of a GeoLas excimer laser with a microscope and an Agilent 7500c quadrupole ICP-MS. LA-ICP-MS analysis was performed to quantify the major elements in the fluid, including [Ca^{2+}], [Mg^{2+}] and [Fe_{tot}]. The quantification of chemical elements was achieved using calibration with aqueous single element solutions (liquid standards) loaded in pure silica capillaries with internal diameter of 320 μm. The same capillaries were used for our fluid analyses. The concentration of liquid standards was chosen depending on the concentration of the initial fluid. For example, initial concentration in Ca is 47 mg/L, thus three liquid standards were chosen of concentration 10 mg/L, 100 mg/L, and 1000 mg/L. Concentration of liquid standards allowed us to plot suitable calibration curves for each element in the range of their plausible concentration in the output fluid.

Ion chromatography (IC) analyses were carried out on some selected solutions with a Metrohm 882 Compact IC plus instrument equipped with a chemical suppression module and a conductivity detector. IC analyses were performed to quantify the carbonate ions in the output fluids.

2.4.2. Petrographical Analyses

To quantify mineralogical transformations in the samples after the creep experiments, the following petrographical analyses were performed: optic microscopy, cathodoluminescence on polished sections, and scanning electron microscopy (SEM). After the creep experiments, the samples were cut lengthwise. Half of each sample was prepared into polished thin sections for observation under an Olympus BX50 microscope and cathodoluminescence (Cambridge instrument technology Ltd (CITL) cold cathode instrument CL8200 Mk4; 500 ± 10 μA gun current and 15 ± 0.5 kV voltage). The second half was used for SEM observations after the creep experiments (SEM observations were also performed before the creep experiments on rock cuttings taken close to the tested core sample) and both secondary electron and backscattered electron modes were used. Chemical characterizations were also performed on these samples using the EDS (energy-dispersive X-ray spectroscopy) method.

2.4.3. Petrophysical Analyses

The intrinsic water permeability k of the sample was measured continuously during the triaxial multistep creep tests (Experiments II and III) using the Darcy's law:

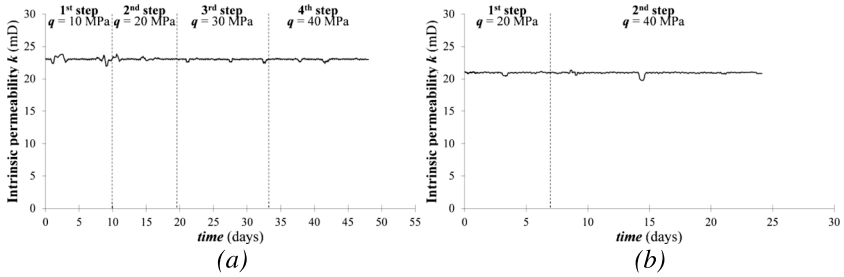

Figure 5. Evolution of intrinsic water permeability *k* during multistep creep tests (Pc = 60 MPa and Pi = 30 MPa). (a) Experiment II: dynamic percolation of the meteoric water. (b) Experiment IV: dynamic percolation of the meteoric water enriched in phosphates.

$$k(t) = \frac{\mu L Q}{S \Delta P(t)} \tag{2}$$

In this equation, L represents the length of the sample (meter), S is the section of the cylindrical sample (square meter), Q is the volumetric flow rate ($m^3\ s^{-1}$), $\Delta P(t)$ is the interstitial pressure drop (0.5 MPa) between the inlet (30.5 MPa) and the outlet (30 MPa) of the sample, and μ represents the dynamic viscosity of the liquid (Pa s^{-1}). Permeability values are reported in Darcy units (1 darcy = $9.8692 \times 10^{-13}\ m^2$).

To characterize the evolution (compared to the initial rock) of the porosity and the shape of the porous network, mercury intrusion porosimetry (Purcell test) was used. Two Purcell tests were performed on each tested sample after the creep experiments.

2.5. Thermodynamic Modeling

Thermodynamic simulations were performed in order to determine the saturation state of the experimental fluids with respect to calcite. We used the PHREEQC V2.18 geochemical software package [*Parkhurst and Appelo*, 1999], together with its Lawrence Livermore National Laboratory database [*Johnson et al*., 2000] with thermodynamic constant only valid at 80°C and 1 bar (0.1 MPa). PHREEQC is a computer program for speciation, batch-reaction, one-dimensional transport, and inverse geochemical calculations. Calcite was the only component of the rock sample used in the calculation of the saturation state. This is a realistic approximation since ICP-ES chemical analysis on rock powder showed the predominance of calcite in the rock sample (Table 1). The carbonate concentration was not well constrained in the output fluid probably because the sampling technique we used do not guarantee the absence of CO_2 reequilibration. Thus, it was not possible to recalculate the calcite saturation index at 80°C from the partial information we had on the output fluid chemistry. Therefore, we have artificially equilibrated an initial fluid (Table 3) with calcite at 80°C, playing with the calcite saturation index and having for constraint to get the measured pH and Ca concentration in the output fluid at the end of each differential stress increment. We have also taken into account the thermodynamic model developed by *Duan and Li* [2008] for the H_2O-CO_2-NaCl system in order to discuss our experimental results in the light of a more appropriate model at high pressure.

3. Results

3.1. Permeability and Porosity Evolutions

Because Experiment I was performed without fluid circulation, permeability was obviously not monitored. Changes in permeability with time and differential stress for Experiments II (flow-through experiment with the meteoric water) and IV (flow-through experiment with the meteoric water enriched in phosphates) are reported in Figure 5. The permeability did not evolve significantly during all experiments: k (initial) ~ 25 mdarcy, k (Experiment II) ~ 23 mdarcy, k (Experiment III) ~ 24 mdarcy, and k (Experiment IV) ~ 21 mdarcy.

The results of mercury porosimetry on the samples after Experiments I, II, III, and IV are reported in Table 2 and total porosity measurements (using a helium pycnometer). A representative porosity spectrum is presented in Figure 2 for the samples after Experiments I, II, and IV. After Experiment I (closed and no-flow condition), the porosity did not change significantly (cf. Figures 2a and 2b); the bulk (total) porosity decreased from 18.6% (initial value) to 16.9%, and the porous spectrum still shows a widespread and multimodal (with a slight bimodal tendency) distribution of pore throat size. After Experiment II (dynamic percolation of the meteoric water), the porosity showed significant changes (Figure 2c) compared to the initial state (Figure 2a).

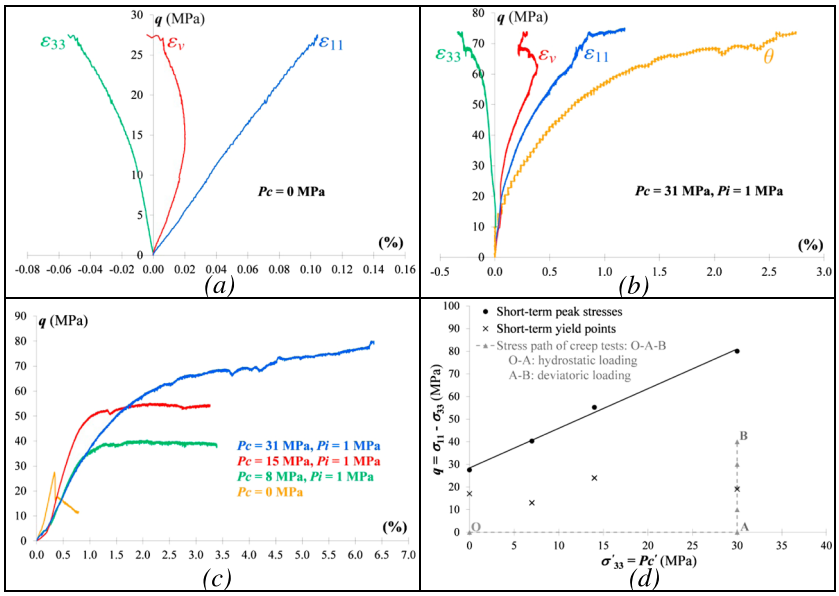

Figure 6. Short-term uniaxial and triaxial compression tests on Massangis limestone at $T = 80°C$. (a and b) Stress–strain curves obtained with strain gauges. (c) Stress-axial strain curves obtained with external LVDT sensor. (d) Short-term peak and yield points and loading path of the triaxial multistep creep tests in the space of effective stresses.

First, the total porosity decreased strongly from 18.6% to 6.5%. Second, pores of entrance radii of less than 0.3 μm in size were no longer detected. This complete disappearance of microporosity in the porous spectrum was measured after both creep Experiments II and III (after each experiment, two mercury injection tests were performed to confirm results). Also, after Experiment IV (dynamic percolation of the meteoric water enriched in phosphates), the total porosity and the porous spectrum did not evolve significantly (Figure 2d) compared to the initial sample (Figure 2a). In all cases, density of solid matrix and total porosity did not change significantly after creep experiments (Table 2).

3.2. Mechanical Data

Let the strain tensor be additively decomposed into time-independent elastic, short-term (i.e., quasi-instantaneous) plastic and creep/viscoplastic (i.e., time dependent) components:

$$\underline{\underline{\varepsilon}} = \underline{\underline{\varepsilon}}^{e} + \underline{\underline{\varepsilon}}^{p} + \underline{\underline{\varepsilon}}^{cr} \tag{3}$$

Under axisymmetric compression, the volumetric strain is

$$\varepsilon_v = \varepsilon_{11} + \varepsilon_{22} + \varepsilon_{33} = \varepsilon_{11} + 2\varepsilon_{33} \tag{4}$$

Thereafter, only the creep components of the strain (ε_{11}^{cr}, ε_{33}^{cr}, and ε_v^{cr}) will be represented in the deformation curves of creep Experiments I, II, III, and IV.

Figures 6a and 6b show stress–strain curves of short-term uniaxial and triaxial compression tests performed on Massangis limestone under drained condition at $T = 80°C$. We also measured the porosity evolution θ during triaxial tests through the monitoring of the volume of exchanged interstitial fluid (drained condition). It is always difficult to compare directly θ with the volumetric strain ε_v measured with strain gauges because the measurement techniques are very different and magnitude of results often differs. It is worth emphasizing that the porosity decrease θ during the short-term triaxial test (Figure 6b), performed at the same effective confining pressure (30 MPa) as for the triaxial multistep creep tests, is only about 0.5% for $q = 40$ MPa. Hence, the decrease in porosity measured with Hg porosimetry cannot stem from a compaction effect due to the increase in differential stress.

The mechanical behavior of the Massangis limestone in triaxial compression depends strongly on the confining pressure as for most porous rocks. Indeed, as confining pressure increases, the mechanical behavior changes from brittle and dilatant to ductile and contractant, as already observed on many porous

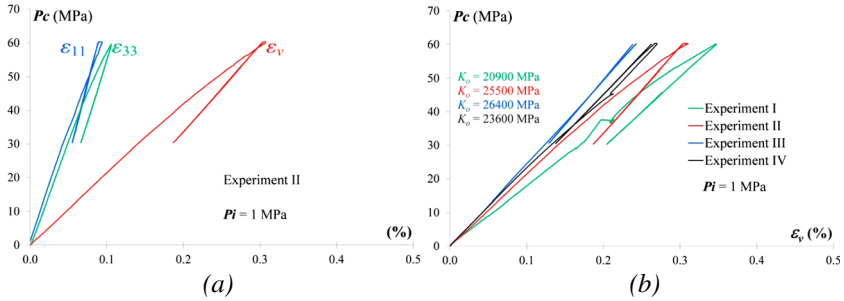

Figure 7. (a) Hydrostatic loading before the multistep creep test II on Massangis limestone: stress–strain curves. (b) Hydrostatic loadings before all multistep creep tests on Massangis limestone: stress-volumetric strain curves.

rocks [e.g., *Elliott and Brown*, 1985; *Wong and Baud*, 2012]. Figure 6c shows the axial curves of all short-term tests obtained with the external LVDT sensor which allows the measurement of the axial deformation even at high stresses for which deformations are localized (i.e., behavior close to the peak stress or postpeak). As confining pressure increases, the plastic behavior of the Massangis limestone changes from strain softening to perfect plasticity and work hardening. The drained Young's modulus is about 55,000 MPa, and the drained Poisson's ratio is about 0.23. The water porosity under vacuum, which is the best technique for the determination of the connected porosity, was measured on each sample before the short-term triaxial tests. We obtained 20.2 ± 0.5% for the four tested samples. This low standard deviation suggests that samples are homogeneous. In addition, this value is close to the values measured with Hg (mercury) porosimetry on the initial sample before creep testing (Figure 2a and Table 2).

Figure 6b shows stress–strain curves of the short-term triaxial compression test with Pc = 31 MPa and Pi = 1 MPa on the Massangis limestone. Therefore, the effective confining pressure Pc' was of 30 MPa, i.e., the same effective confining pressure as for the triaxial multistep creep tests (Experiments I, II, III, and IV). For this high confining pressure, the mechanical behavior is contractant and work hardening (Figure 6c). The short-term dilatancy threshold (i.e., the onset of the dilatant volumetric deformation), which corresponds to the onset of unstable propagation of microcracks [*Bieniawski*, 1967] and therefore to the long-term strength (i.e., onset of tertiary creep), is not visible in this test. Figure 6d represents the short-term peak and yield points and the loading path of the triaxial multistep creep tests in the space of effective stresses. It is worth emphasizing that since the behavior of the Massangis limestone changes from brittle and dilatant to ductile and contractant as confining pressure increases, the extent of the linear portion of the axial strain curves decreases with increasing confining pressure, making it more difficult to define the yield points. Anyway, as shown by Figure 6d, during creep Experiments I, II, III, and IV, the material was held at a differential stress q up to 40 MPa which corresponds approximately to half of its short-term peak stress. Therefore, differential stresses from 20 MPa to 40 MPa are above the short-term yield point and are sufficiently high to activate chemomechanical processes such as PSC and/or subcritical cracking but too low to induce the long-term failure (i.e., tertiary creep) of the material.

Figure 7a represents the stress–strain curves of the hydrostatic loading before the multistep creep test II on Massangis limestone. This figure shows that under hydrostatic loading, the material behavior is isotropic ($\varepsilon_{11} \sim \varepsilon_{33}$) and almost elastic. Indeed, no pore collapse mechanism is observed in the volumetric strain curve. Figure 7b shows volumetric strain curves of the hydrostatic loadings before all multistep creep tests on Massangis limestone. At Pc = 60 MPa, an unloading-reloading cycle was performed (i.e., the confining pressure Pc was half unloaded) to determine the drained bulk modulus K_o. As the values of K_o are quite similar, samples can be considered as homogeneous from a mechanical point of view. This is an important consideration since the multistep creep experiments will be compared with one another.

Figure 8 shows deformation curves (axial, lateral, and volumetric strains versus time) of all multistep creep tests. The classical creep stages (i.e., primary/transient and secondary) can be observed in the axial creep curves but especially in Experiments II and III (dynamic percolation of the meteoric water) and for the higher

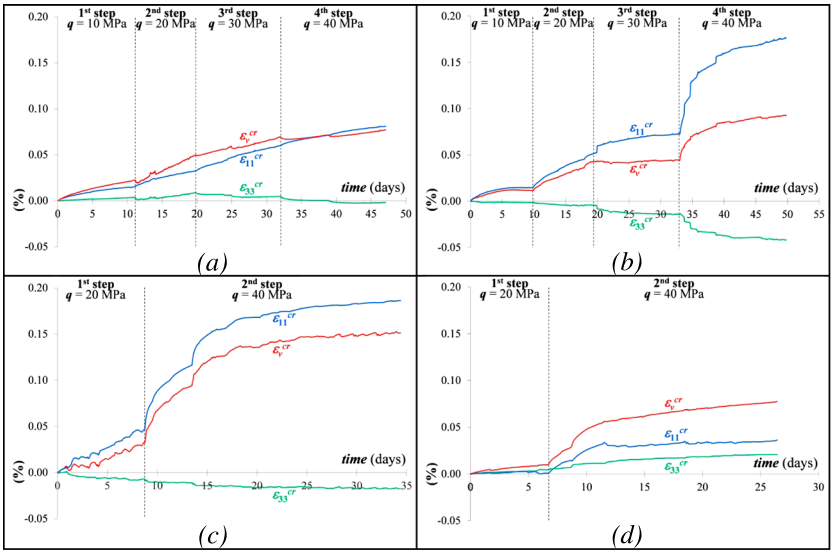

Figure 8. Deformation curves (axial, lateral, and volumetric strains versus time) of multistep creep tests (Pc = 60 MPa and Pi = 30 MPa). (a) Experiment I: sample saturated with meteoric water without circulation (i.e., closed and no-flow condition). (b) Experiment II: dynamic percolation of the meteoric water with four stress increments. (c) Experiment III: dynamic percolation of the meteoric water with two stress increments. (d) Experiment IV: dynamic percolation of the meteoric water enriched in phosphates.

stress levels. In all experiments, the axial strain increases with time and differential stress q and is much higher than the lateral strain which results in material compaction/contraction (i.e., positive volumetric strain). It is worth emphasizing that deformations measured during all experiments are not very significant, which is in good agreement with this kind of hard rock (see the intrinsic mechanical properties of the Massangis limestone, Figures 6 and 7). In addition, for creep Experiments II and III, the volumetric compaction measured with strain gauges (Figures 8b and 8c) is very limited (~ 0.1%). Hence, the decrease in porosity measured with Hg porosimetry cannot stem from a compaction effect due to the increase in differential stress.

3.3. Chemical Data

Because Experiment I was performed without fluid circulation (i.e., closed and no-flow condition), fluid sampling was not possible during this test. So chemical analyses were only performed on the initial fluid used for the saturation and on the interstitial fluid at the end of the experiment. The results, compiled in Table 3, show a significant increase in calcium and iron concentrations at the end of the test. Calcium concentration is 3 times larger at the end of the experiment when compared to the initial fluid. Conversely, the magnesium concentration in the final fluid is almost 3 times lower than in the initial fluid. The carbonate ion CO_3^{2-} shows an increase from 36.2 mg/L to 49.8 mg/L. The pH of the output fluid shows a small decrease from 7.62 to 6.92 (Table 3).

The Experiment II was performed under flow-through conditions (dynamic percolation of the meteoric water with four differential stress increments), allowing the output fluid to be sampled regularly during the experiment. Analyses of Ca, Mg, and Fe concentrations and pH in the percolating fluid are reported in Figure 9 and Table 3. Under hydrostatic loading (i.e., before the creep test and the application of the differential stress q), the composition of the output fluid did not change significantly compared to the initial fluid (used for the saturation of all samples). During the multistep creep test, the concentrations of calcium, iron, and carbonate ions in the output fluid increased with time and differential stress. Despite the variation in the measured values, $[Ca^{2+}]$ and $[Fe_{tot}]$ seems to follow the evolution of the axial strain curve (Figure 8b). At $q = 40$ MPa, the calcium concentration reached 250 mg/L, which is 5 times the initial concentration. Conversely, the magnesium concentration decreased strongly and remained below the detection limit of LA-ICP-MS (< 5 ppb). During Experiment II, pH values of the output fluid did not vary significantly compared to the initial fluid (Figure 9d and Table 3).

The Experiment III was also performed under flow-through conditions (dynamic percolation of the meteoric water), allowing the output fluid to be sampled regularly. In this experiment, only two differential stress increments were performed compared to the four stress increments of the Experiment II. As for Experiment II,

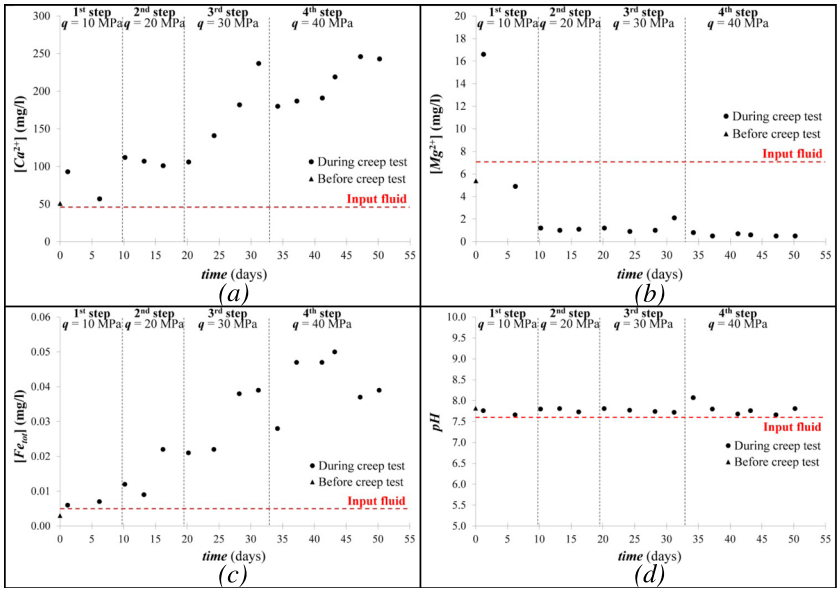

Figure 9. Evolution of the concentration of dissolved (a) calcium, (b) magnesium, (c) iron, and (d) pH of the output fluid during the Experiment II (dynamic percolation of the meteoric water with four stress increments).

the concentrations of calcium and iron ions in the output fluid increased with time and differential stress and the magnesium concentration decreased (Figure 10). $[Ca^{2+}]$ and $[Fe_{tot}]$ also reproduce the evolution of the axial strain curve (Figure 8c). At $q = 40$ MPa, the calcium concentration reached 210 mg/L, which is close to the concentration obtained at the end of the Experiment II (250 mg/L). pH did not evolve significantly during this experiment.

The Experiment IV was also performed under flow-through conditions (i.e., dynamic percolation), but the meteoric water was enriched in phosphates. Unlike the other Experiment I, II, and III, the concentrations of Ca, Mg, and Fe ions in the output fluid did not show a noticeable evolution with applied differential stress q and time (Figure 11). As for all experiments, pH did not evolve significantly.

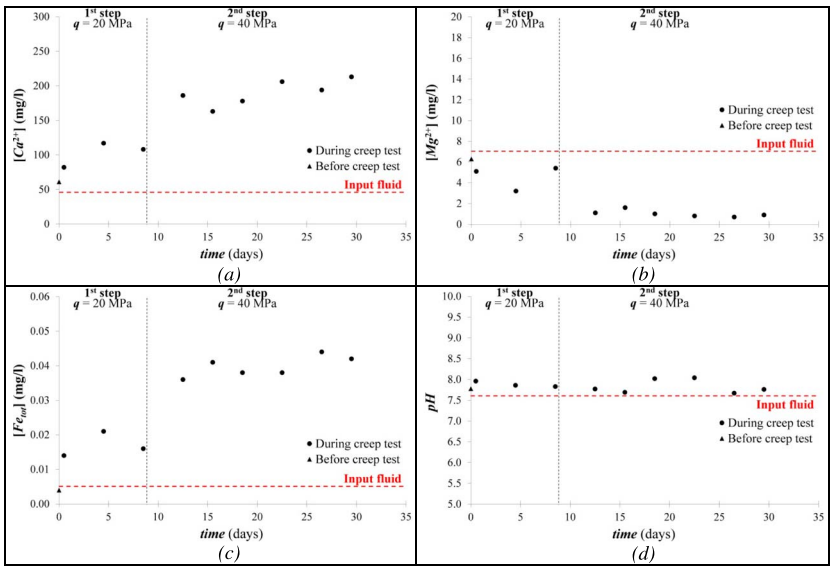

Figure 10. Evolution of the concentration of dissolved (a) calcium, (b) magnesium, (c) iron, and (d) pH of the output fluid during the Experiment III (dynamic percolation of the meteoric water with two stress increments).

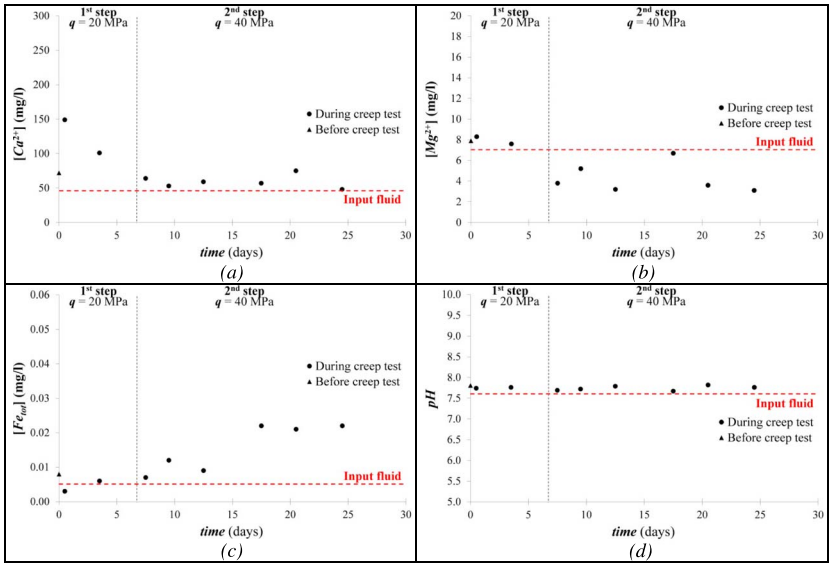

Figure 11. Evolution of the concentration of dissolved (a) calcium, (b) magnesium, (c) iron, and (d) pH of the output fluid during the Experiment IV (dynamic percolation of the meteoric water enriched in phosphates).

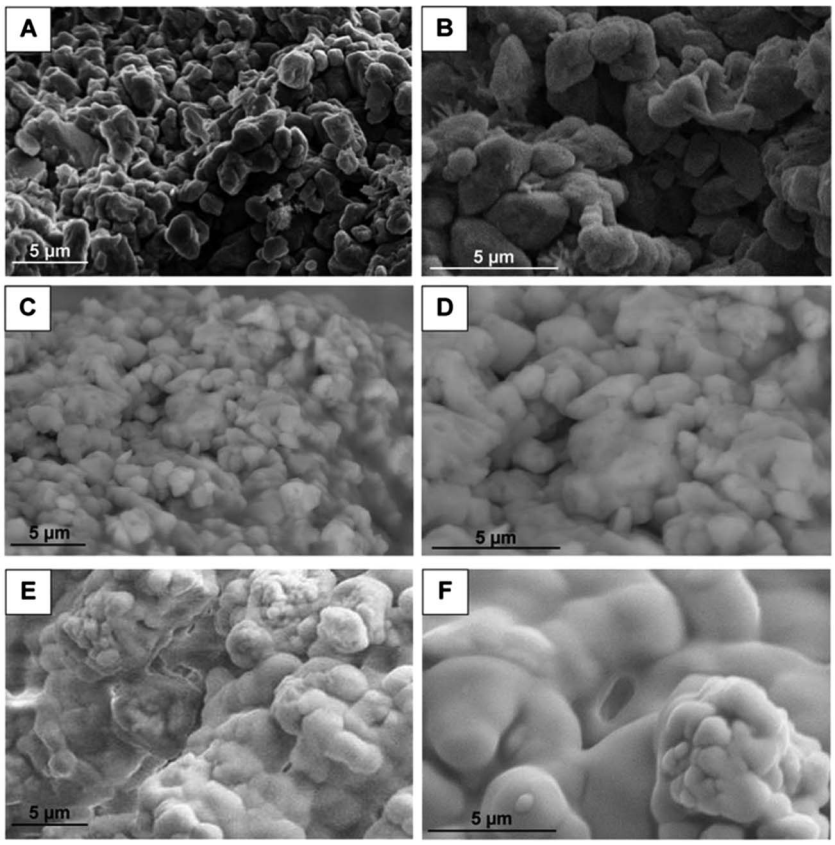

Figure 12. SEM observations on Massangis limestone showing micritic crystals. (a and b) The initial rock before experimentation. (c and d) The rock after the Experiment I (closed and no-flow condition). (e and f) The rock after the Experiment II (dynamic percolation of the meteoric water) and precipitation of calcite on micritic crystals.

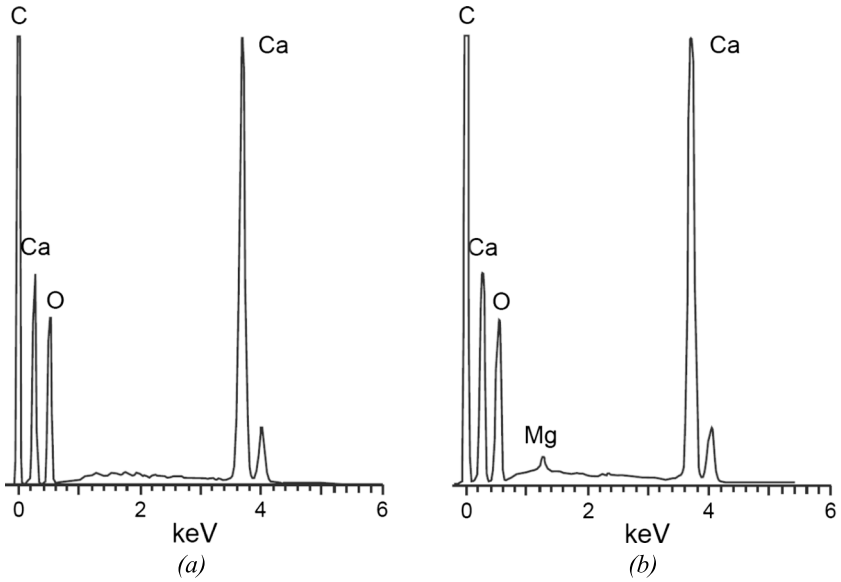

Figure 13. EDS spectra of micrites in the (a) initial sample and (b) after Experiment II.

3.4. Petrographical Observations

At the end of each creep experiment, the petrography of the tested samples was analyzed and compared with the initial rock. There were no changes observed at the scale of optical microscopy and cathodoluminescence analyzes. However, SEM observations showed alterations in the morphology micrite crystals. Figure 12 represents a selection of SEM images obtained on the initial rock before experimentation (Figures 12a and 12b) and on the samples after Experiments I (Figures 12c and 12d) and II (Figures 12e and 12f). Micrites can be described according to the classification of *Deville de Periere et al.* [2011]. Micrites in the initial rock display subrounded to microrhombic shapes with punctic and sometimes partially coalescent contacts (Figures 12a and 12b). Changes in micrite crystals are more significant in the flow-through Experiment II than in the no-flow Experiment I. Indeed, micrites after Experiment I are subrounded to rounded with predominantly coalescent and sometimes punctic contacts (Figures 12c and 12d). After Experiment II, micrite crystals show a drastic change in their shape and contacts; they are rounded to fuse with fully coalescent contacts (Figures 12e and 12f). EDS analysis indicated the presence of calcium without magnesium above the limit of detection in the initial rock (Figure 13a). After the Experiment II, EDS analysis on the tested sample showed an increase in the magnesium content of micrites (Figure 13b).

4. Discussion

4.1. Time-Dependent Deformation Mechanisms

Under the stresses/temperature conditions of DBR (relatively high temperature, high confining, and differential stresses), many deformation mechanisms may be invoked to explain the long-term deformation of Massangis limestone. First, cataclastic (or microbrittle granular) flow is a mechanism that describes the permanent straining achieved by the relative movement of the fragments of the broken material [*Paterson and Wong*, 2005]. If the initial porosity of the material is important, the classical tendency to dilatancy of porous rocks during creep deformation may be counter-balanced through collapse of its porosity and cataclastic flow may thus be accompanied by compaction rather than dilation, as suggested by *Paterson and Wong* [2005]. In our creep experiments, cataclastic flow and pore collapse mechanisms can be discounted based on the absence of fragmented grains (crystals) under SEM observation after creep testing and the absence of significant compaction during the creep deformation (Figure 8). In addition, the effective stress during our creep tests on the Massangis limestone was probably too low for cataclastic flow to have taken place, as suggested by many authors [e.g., *Baud et al.*, 2000; *Vajdova et al.*, 2004, 2010; *Schubnel et al.*, 2005]. Figure 7, which represents hydrostatic loadings before each multistep creep test on Massangis limestone, also shows that there is no pore collapse mechanism under an effective confining pressure of 60 MPa.

Second, subcritical crack growth is another mechanism, resulting in the static fatigue (i.e., time-dependent brittle behavior) of rocks, which could be invoked to interpret our experiments. Indeed, this deformation mechanism is enhanced by the presence of water through physiochemical reactions at crack tips, e.g., stress corrosion in the case of silicate rocks [e.g., *Atkinson*, 1984; *Atkinson and Meredith*, 1987; *Scholz*, 1968]. In the case of deformation of calcite rocks in the temperature range 20–500°C, *Rutter* [1974] suggested that there is no evidence that stress corrosion, as described for quartz and other silicates, plays any role. Indeed, this hydrolytic weakening is unlikely to be important in the deformation of ionic crystals such as calcite. In the presence of aqueous fluids, many other mechanisms may be involved in the subcritical cracking of rocks, namely, dissolution, diffusion, ion exchange, and microplasticity [*Atkinson*, 1984]. Hence, *Røyne et al*. [2011], *Liteanu and Spiers* [2009], *Croizé et al*. [2010a], and *Brantut et al*. [2013] reported that subcritical microcracking is an active mechanism of long-term deformation in carbonate rocks. However, *Zhang and Spiers* [2005a, 2005b], in their studies of time-dependent behavior of calcite aggregates in the presence of aqueous fluids, have discounted the subcritical cracking mechanism on the basis of the absence of acoustic emissions during their experiments. In addition, the absence of significant lateral deformation and thus dilatancy (due the opening of axially oriented microcracks, i.e., in the direction of the major principal stress σ_{11}) during both short-term (Figure 6b) and creep (Figure 8) tests and the constancy of the permeability during all creep tests (Figure 5) indicates that subcritical cracking is not of great importance in all our experiments. Indeed, Figures 6b and 6c show clearly that for the high effective confining pressure (30 MPa) of triaxial creep tests, the mechanical behavior is ductile and contractant.

Yet all our analyses indicate that active processes occurred at the micritic scale. Chemical analyses showed a complex evolution of the output fluid composition with time and differential stress q (Figures 9–11). Taken separately, the increase in calcium concentration with time and differential stress q may be due to a combination of kinetic dissolution and thermodynamic properties of Ca-bearing phases at high pressure. But taken together with mechanical (axial compaction, Figure 8), petrophysical (decrease in porosity, Figure 2c and Table 2), and petrographical (change in the shape of micrite crystals, Figure 12) analyses, chemical results suggest rather a PSC process. In addition, the adjunction of phosphate ions in the percolating meteoric water (Experiment IV: dynamic percolation) inhibits the Ca release in the output fluid (Figure 11a), the decrease in porosity (Figure 2d and Table 2) and the axial contraction (Figure 8d). This is another evidence of the PSC process occurrence inasmuch as the inhibiting effects of phosphate ions on intergranular pressure solution in calcite are well known [e.g., *Zhang and Spiers*, 2005b]. Amongst all time-dependent deformation mechanisms, PSC is therefore the most likely in carbonate rocks such as Massangis limestone.

The PSC mechanism and its application to Experiments I and II are described schematically in Figure 14. PSC is a coupled chemomechanical process that causes particles, such as grains (or crystals in our case), to come closer as a response to increased axial stress (Figure 14b), thus generating an increase in normal stress at grain contacts. The equilibrium constant of the dissolution-precipitation reaction is greater at contact points between crystals than at free faces [*Rutter*, 1976; *Zubtsov et al*., 2004; *Van Noort et al*., 2008; *Yasuhara et al*., 2003; *Paterson*, 1973]. This leads to a progressive local dissolution of solid material (i.e., crystal matter) at crystal contacts. The solutes (Ca and Fe ions) are transported out of the contacts by diffusion through the fluid film between crystals according to the theory of "Water Film Diffusion" proposed by *Weyl* [1959], *Rutter* [1976], and *Gunzburger* [2010], as shown in Figure 14b. Pressure solution occurs between micrite crystals at the microscopic scale (Figure 12), and this dissolution explains the increase in axial strain (i.e., contraction or compaction) during all experiments (Figure 8). PSC being a slow, time-dependent mechanism [e.g., *Dysthe et al*., 2006], it is understandable that the petrographical evidences (Figure 12) can be observed at a scale no greater than that of micrite crystals. After dissolution of crystal matter, the solutes (Ca and Fe ions) precipitate on the less stressed faces of grains or crystals [e.g., *Rutter*, 1976; *Zubtsov et al*., 2004]. The calcite precipitations on pore walls integrate magnesium from the percolating fluid, as schematically illustrated in Figures 14c and 14d, which explains the decrease in $[Mg^{2+}]$ in the interstitial fluid (Table 3 and Figures 9 and 10).

4.2. Effects of Stress, and Chemistry and Flow Condition of Pore Fluid on the PSC Process

4.2.1. Effects of Stress

The intensity of the PSC process increases as a function of axial stress. This can be seen in mechanical data of creep experiments (Figure 8). While lateral strains remain not significant in all experiments, axial strains increase (i.e., contraction) with applied differential stress q. Experiments II and III, which were performed

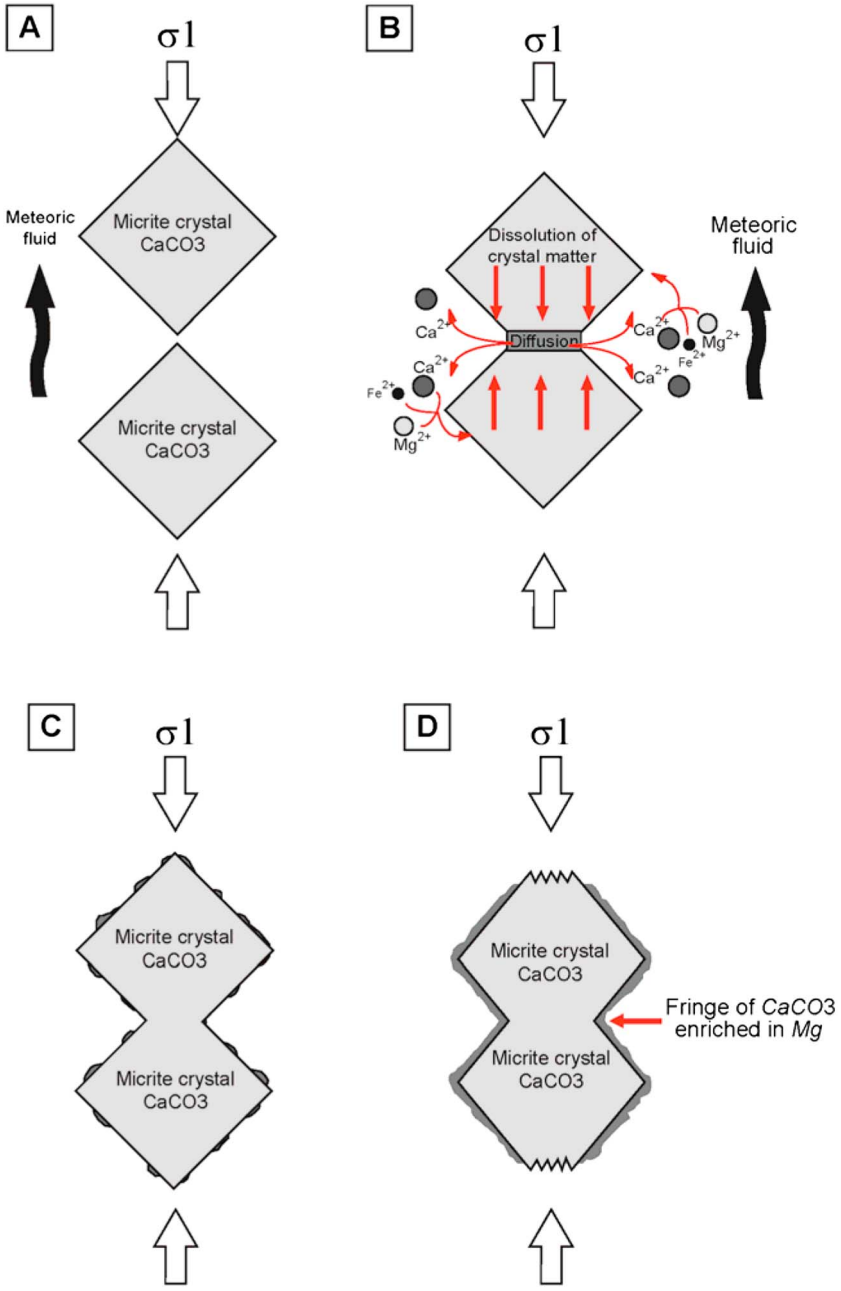

Figure 14. Schematic representation of the pressure solution process and its application to experiments. (a) Before the beginning of the process. (b) In process. (c) Final state of micrites after Experiment I (closed and no-flow condition). (d) After Experiments II and III (dynamic percolation of the meteoric water). Modified from *Van Noort et al.* [2008] and *Yasuhara et al.* [2003].

under the same flow conditions (dynamic percolation of the meteoric water), display the largest axial deformations. At the end of the last stress level ($q = 40$ MPa), the axial deformation corresponds to 0.18% in both cases. This suggests that the maximal axial deformation the material can reach at a given stress level does not depend on the stress path (four stress increments in Experiment II and two stress increments in Experiment III). Experiment IV, which was performed with a dynamic percolation and continuous renewal of the meteoric water enriched in phosphates, displays the lowest axial deformations (~ 0.035% at the end of the last stress level). Experiment I, which was performed with meteoric water without circulation (i.e., closed and no-flow condition), also displays low axial deformations (~ 0.08% at the end of the last stress level). Hence, the maximal axial contraction (or compaction) at the end of the last stress level ($q = 40$ MPa) depends

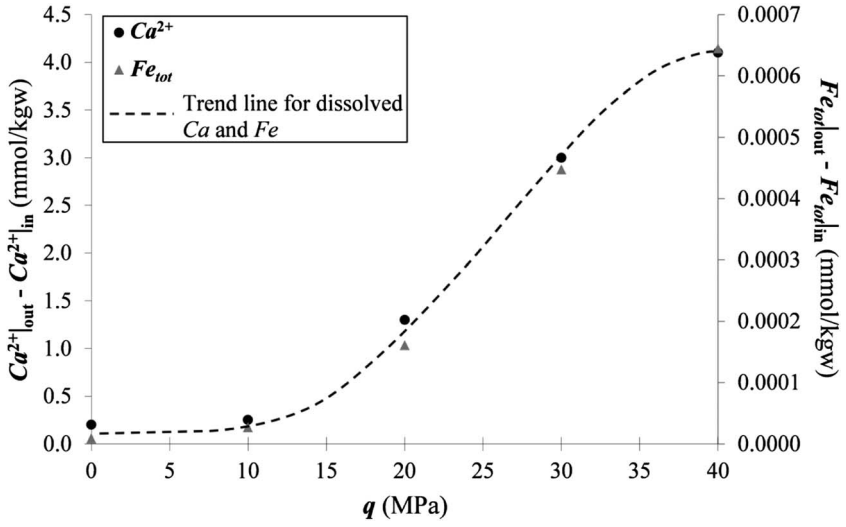

Figure 15. Relationship between differential stress q and mean dissolved Ca^{2+} and Fe_{tot} in the output fluid during Experiment II (dynamic percolation of the meteoric water with four stress increments). $Ca,Fe|_{out}$ = quantity of Ca and Fe in the output solution; $Ca,Fe|_{in}$ = quantity of Ca, Fe in the input solution.

on the flow conditions and the chemical compositions of the fluid. The remaining question is where is the system going? For the last stress level ($q = 40$ MPa) during the secondary stage of creep, the axial strain rate of creep is $d\varepsilon_{11}^{cr}/dt = 1.5 \times 10^{-8}$%/s (Experiment I), 1.9×10^{-8}%/s (Experiment II), 1.4×10^{-8}%/s (Experiment III), 4.5×10^{-9}%/s (Experiment IV). Hence, the axial strain rate is almost equal in the first three experiments but is 3–4 times lower in the Experiment IV with phosphates, thus illustrating again inhibiting effects of phosphate ions on intergranular pressure solution in calcite. However, secondary creep is not completely stabilized in all experiments (inter alia because of the relatively short duration of this stress step) and these values of creep strain rate should be taken carefully. While the first two creep stages (i.e., primary/transient and secondary) can be observed in Figure 8, especially in Experiments II and III (dynamic percolation of the meteoric water) and for the higher stress levels, tertiary (i.e., accelerated) creep was not observed in any experiment. Two hypotheses may be invoked to explain this. First, if PSC is the main mechanism in our creep experiments, we are actually not supposed to see this third creep stage and eventually long-term brittle failure. Indeed, we are not in the brittle regime but rather in the ductile regime, as illustrated by Figures 6b–6d. Second, the differential stress was not high enough. Indeed, as illustrated in Figures 6b–6d, even at the last stress level ($q = 40$ MPa), the differential stress represents only 50% of the short-term peak stress.

The impact of stress increase on the intensity of the PSC process can also be seen in chemical data (Figures 9–11). Indeed, as for axial strain, the increase in calcium and iron concentrations in pore fluid is correlated with the increase in differential stress q in all experiments, except for Experiment IV (dynamic percolation of the meteoric water enriched in phosphates). For example, the chemical analysis (Figure 9b and Table 3) of the output fluid during Experiment II (dynamic percolation of the meteoric water with four stress increments) showed that $[Ca^{2+}]$ is 5 times higher at $q = 40$ MPa than at $q = 0$ MPa (i.e., before creep test). This chemical analysis also showed a sudden and punctual increase in both calcium and magnesium concentration. This sudden release of dissolved matter can be explained by the heterogeneity of the sample and the porous network. It is questionable that this value represents a real variation of matter dissolution rate. Therefore, it will not be integrated in any further modeling.

Figure 15 demonstrates for Experiment II the positive correlation between differential stress q and dissolved Ca and Fe in the output fluid. The Ca/Fe concentration ratio (in mmol/kgw) in the initial rock is of 200 (Table 1), while in the output fluid this ratio is 6000 at the end of the experiment (Figure 15). This can be explained by the fact that only a small fraction of iron of the rock, which comes mainly from pyrite crystals, is integrated in micrite crystals (representing the ratio found in the output fluids). The positive correlation between differential stress q, $[Ca^{2+}]$ and $[CO_3^{2-}]$ (Table 3) hints toward an increase of the dissolution process but not of the precipitation process. Thus, there is an evident relationship between (i) the porosity that affects both the water flow path and the diffusion processes, (ii) the thermodynamic of water/rock interactions at

Table 4. Quantities of Dissolved $CaCO_3$ in Experiments I and II, Calculated From Fluid Analysis (cf. Table 3)[a]

	Differential Stress q (MPa)	Test Duration (day)	Volume of Injected Fluid (mL)	Mean Dissolved Ca^{2+} (mg/L)	Dissolved Ca^{2+} (mg)	Dissolved $CaCO_3$ (mg)
Experiment I	0–40	55	20	104	2.08	5.2
Batch theory	-	-	20	1	0.02	0.05
Experiment II	0	8	153	8	1.2	3
	10	11	211	28	5.9	14.75
	20	9	173	52	9	22.5
	30	13	250	120	30	75
	40	19	365	164	59.8	149.5
Total			1152	-	106	264.75
Batch theory	-	-	1152	1	1.152	2.88

[a]In theoretical batch experiments, quantities were calculated from the fluid-rock equilibrium state.

high pressure/stresses, and (iii) the crystallographic constraints. All these parameters drive the nature, kinetic, and equilibriums of the dissolution-precipitation reactions occurring in this dynamic and complex porous network.

4.2.2. Effects of Chemistry and Flow Condition of Pore Fluid

The intensity of the PSC process is higher in Experiments II and III (flow-through condition with four and two stress increments, respectively) than in Experiment I (closed and no-flow condition). The dissolution of solid matter (assumed to be $CaCO_3$ only) was of 5.2 mg at the end of the Experiment I and 264.75 mg at the end of the flow-through Experiment II (Table 4). These values were calculated on the basis of the volume of the injected fluid and its Ca concentration at the sample output (cf. fluid analysis in Table 3). However, this large difference in the amounts of dissolved $CaCO_3$ may stem from the difference in the volume and flow condition of the fluid that reacted with rock (Table 4), i.e., 20 mL in Experiment I (corresponding to the pore volume filled by the meteoric water, without circulation) and 1152 mL in Experiment II (dynamic percolation). This difference may be explained by two processes. First, fluid flow increases the rate of circulation of solid matter [*Bjørlykke and Høeg*, 1997]. The second process corresponds to the progressive reaching of a saturation state of calcite in the interstitial fluid, in the Experiment I (closed and no-flow condition). The fluid being constantly renewed in Experiment II, the saturation state was never reached thus leading to a continual dissolution process. In addition, the decrease in the Mg concentration in output fluids (Table 3 and Figures 9b and 10b) and petrographical observations; i.e., the formation of a calcite layer enriched in Mg on micrite crystals (Figure 12), after Experiments I, II, and III suggest the occurrence of a precipitation process. This precipitation process is more important in the Experiments II and III than in the Experiment I, as noticeable by petrographical observations (Figure 12).

Numerous experimental studies [e.g., *Reddy*, 1977; *Dove and Hochella*, 1993; *Davis et al*., 2000; *Alkattan et al*., 2002; *Plant and House*, 2002] have shown that the presence of phosphate ions in the pore fluid reduces reaction rates of both carbonate dissolution and precipitation. In the experimental study of *Zhang and Spiers* [2005b] on calcite powders, done by the way of uniaxial compaction tests at low applied stresses (1 to 4 MPa), an increase in phosphate concentration in the interstitial fluid led to a significant decrease in pressure solution strain rate, thus evidencing the importance of fluid chemistry on this coupled chemomechanical process. Rate inhibition was credited to be caused by the adsorption of aqueous phosphate on calcite surfaces which are very favorable adsorption sites for aqueous phosphate [*Dekanel and Morse*, 1978]. Consequently, phosphate-bearing ions block active attachment sites, leading to the inhibition of calcite dissolution. In our experimental study, the addition of phosphate ions in Experiment IV induced a significant diminution of calcite dissolution rate (Figure 11) and, thus, of time-dependent axial compaction (Figure 8d), compared to the Experiment III (Figures 10 and 8c) which has been performed under the same conditions (dynamic percolation of the meteoric water with two stress increments). Therefore, our experimental data suggest that PSC is the main time-dependent deformation mechanism in Massangis limestone and that the addition of phosphate ions (phosphate being mainly a component of sea water compared to meteoric/fresh water) in pore fluid inhibits greatly the PSC process. The origin and composition of the pore fluid is therefore very important for the quantification of the rate of the diagenetic process of PSC at great depth.

4.3. Experimental Results Versus Thermodynamic Simulations: Effects of Applied Stress

As presented in section 4.2.2, the dissolution of solid matter (assumed to be $CaCO_3$ only) was estimated on the basis of the volume of the injected fluid and its Ca concentration at the sample output (cf. fluid analysis in

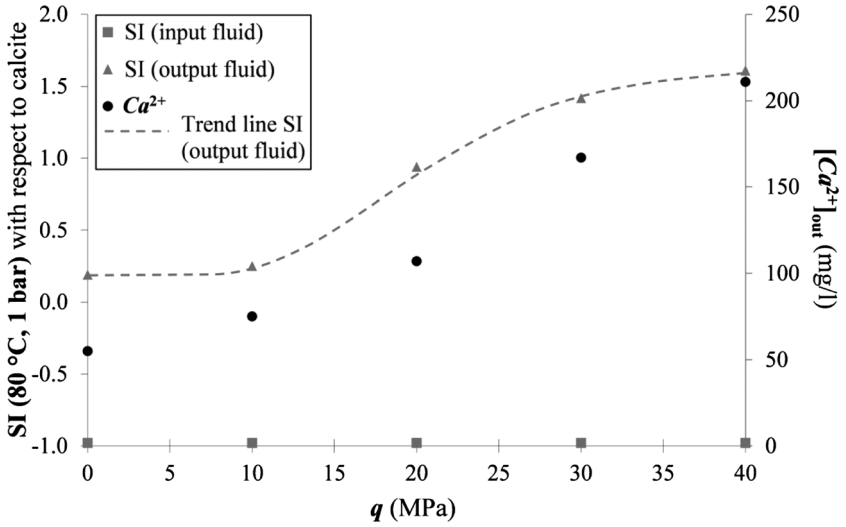

Figure 16. Saturation index (SI) with respect to calcite (logarithmic scale) and concentration of Ca^{2+} in the output fluid versus differential stress *q*. SI was calculated at 80°C and 0.1 MPa with PHREEQC using experimental data (Experiment II: dynamic percolation of the meteoric water with four stress increments).

Table 3). To obtain this estimation, a mean value for dissolved calcium was determined for each level of differential stress. Hence, we obtained (cf. Table 4) from these experimental data 5.2 mg of dissolved calcite (corresponding to 2.08 mg of dissolved calcium) at the end of the Experiment I (closed and no-flow condition) and 264.75 mg of dissolved calcite (corresponding to 106 mg of dissolved calcium) at the end of the Experiment II (flow-through condition). In parallel, we performed batch thermodynamic simulation of calcite solubility with PHREEQC (80°C and 0.1 MPa) which allows a theoretical estimation of dissolved calcite by taking into account the volume of the fluid that reacted with rock during experiments. We obtained from thermodynamic simulation (cf. Table 4) 0.05 mg of dissolved calcite (corresponding to 0.02 mg of dissolved calcium) at the end of the Experiment I and 2.88 mg of dissolved calcite (corresponding to 1.152 mg of dissolved calcium) at the end of the Experiment II. Hence, quantities of dissolved calcite are significantly lower (by a factor of a 100) in thermodynamic simulations than in experimental results. This difference is due to the fact that simple (batch) thermodynamic simulation does not take into account the effect of stresses/pressure on solubility constants and therefore differs greatly from our experimental conditions. Indeed, our experimental results suggest an increase in calcite solubility with stresses, leading to an increase of $[Ca^{2+}]$ in output fluid (Figures 9 and 10 and Tables 3 and 4). To illustrate this effect, we represented in Figure 16 the saturation index (SI) with respect to calcite during Experiment II. SI is calculated as follows:

$$\mathrm{SI} = \log\frac{Q}{K} = \log Q = \log K \tag{5}$$

In this equation, *Q* represents the ion activity product and *K* is the solubility product. Hence, *Q* represents the actual composition of the fluid and *K* represents the composition at chemical equilibrium (when $\mathrm{SI} < 0$ the solution is undersaturated and the mineral may be dissolved; when $\mathrm{SI} > 0$ the solution is supersaturated and the mineral may be precipitated; and when $\mathrm{SI} = 0$ the solution and mineral are at chemical equilibrium). SI was calculated at 80°C and 0.1 MPa with PHREEQC by considering $[Ca^{2+}]$ and pH of the output fluid at the end of each differential stress increment. These data, which were obtained using solubility constant for calcite valid at 0.1 MPa, show clearly that the output fluid becomes highly supersaturated with respect to calcite when *q* increases.

As previously discussed in this paper, PSC seems to be the main process at work. PSC is a pressure-dependent process, as previously demonstrated by many authors [e.g., *Weyl*, 1959; *Spiers et al*., 1990; *Croizé et al*., 2010a] who correlated strain rate due to pressure solution to applied stress. While the calcite solubility is well known under atmospheric conditions [*Plummer and Wigley*, 1976] or is calculated as a function of pCO_2 [*Pokrosky et al*., 2005, 2009], pH [*Plummer et al*., 1978; *Marini*, 2007] and temperature [*Pokrosky et al*., 2009; *Plummer et al*., 1978], its dependence on stresses is neglected in classic thermodynamic calculations. However, it is now known that

the solubility of calcite increases with large stresses, as was demonstrated notably by *Caciagli and Manning* [2003]. Batch thermodynamic simulation of calcite solubility with PHREEQC (80°C and 0.1 MPa), i.e., a software that does not take into account the pressure effect on calcite solubility, returned a value of 0.025 mmol/kgw. The thermodynamic model of *Duan and Li* [2008] is able to calculate coupled phase and aqueous equilibrium of the H_2O-CO_2-NaCl-$CaCO_3$ system up to 250°C and 100 MPa. The calcite solubility in pure water predicted by this model is 0.36 mmol/kgw at 80°C and 100 MPa, i.e., a value 14 times higher than the value obtained with PHREEQC (80°C and 0.1 MPa). However, our experimental data indicate that calcite solubility (based on Ca concentration measurements, cf. Table 4) is higher by almost one order of magnitude than the value obtained with the model of *Duan and Li* [2008], i.e., 2.3 mmol/kgw (Experiment II). These calculations demonstrate that calcite solubility is not only controlled by the global thermodynamic properties PVTX (pressure-volume-temperature-composition) of the system. Other constraints have to be considered, especially those playing a role at the scale of the crystals (crystalographic distortion, local stress, heterogeneous field of pressure…).

This increase in calcite solubility with differential stress may have important geological consequences. Specifically, it may signify that fluids that evolved in deep basins could become progressively less able to hold calcite in solution as they rise to the surface. Accordingly, a considerable amount of calcite may precipitate along the flow path. This precipitation phenomenon may lead to a change in both porosity and permeability during cooling and decompression of basinal fluids. Because the classical geochemical models do not integrate calcite solubility's dependence to pressure/stresses, they may not be suitable for carbonate reservoir modeling. In the future, models would be improved by the addition of pressure solution processes and the dependence of calcite solubility to pressure.

4.4. Effects of PSC on Porosity and Permeability

These results suggest that pressure solution, a process first described by *Sorby* [1863], is the most important mechanism controlling poronecrosis during burial, as shown by many authors [e.g., *Rutter*, 1983; *Tada and Siever*, 1989; *Tada et al*., 1987; *Leythaeuser et al*., 1995; *De Meer et al*., 2002]. In our study, the PSC process induced changes in micrite morphology, as shown in Figures 14c and 14d, and changes in the porous network between micrites (Figure 17). The evolution of the surface morphology of crystals has been previously shown by *Dysthe et al*. [2003]. *Deville de Periere et al*. [2011] established a relationship between the morphology of micrites and their porosity. Micrites of the initial rock being subrounded to microrhombic with punctic contacts, the classification of *Deville de Periere et al*. [2011] indicates porous micrites. The same classification on a sample after Experiment I (closed and no-flow condition) indicates that the micrites are still porous and have only slightly altered access to intercrystal micropores (cf. Figures 12c and 12d), as schematically represented in Figure 17b. Thus, while the morphology of micrite crystals is slightly modified, the microporosity between crystals is preserved, as illustrated by the similarity of porous spectra of the initial sample (Figure 2a) and the sample after Experiment I (Figure 2b).

Conversely, the classification of micrites after Experiments II and III (dynamic percolation of the meteoric water) shows tight micrites with blocked access to the intercrystal micropores. As shown in Figures 12e, 12f, and 17c, the precipitation of a fringe of calcite on free pore walls of micrites blocks the microporosity between micrite crystals, thus inducing a decrease in the mercury connected porosity and complete disappearance of microporosity in the porous spectrum (cf. Figure 2c and Table 2). Actually, the density of the solid matrix and the total porosity of the samples did not change after Experiments II and III (cf. Table 2). However, the microporosity, which is still present in the porous network, was rendered inaccessible to the high-pressure mercury (and probably to any fluid) because of the precipitation of this calcite fringe, thus explaining why it is not visible anymore in the porous spectrum (Figure 2c). The preservation of macropores, which were not affected by the PSC process, allows the preservation of permeability, as illustrated in Figure 5a. The addition of phosphate ions in Experiment IV induced a significant diminution of calcite dissolution rate (Figure 11), thus inhibiting the PSC process. Consequently, porosity (Figure 2d and Table 2) and permeability (Figure 5b) of the tested sample are preserved.

4.5. Practical Implications and Suggestions

The new experimental setup presented here may have several applications for future studies on reservoir rocks. For example, it can be used to test the behavior of consolidated rocks under the high pressure/stresses and temperature conditions of DBR, unlike prior studies which have been performed under simpler

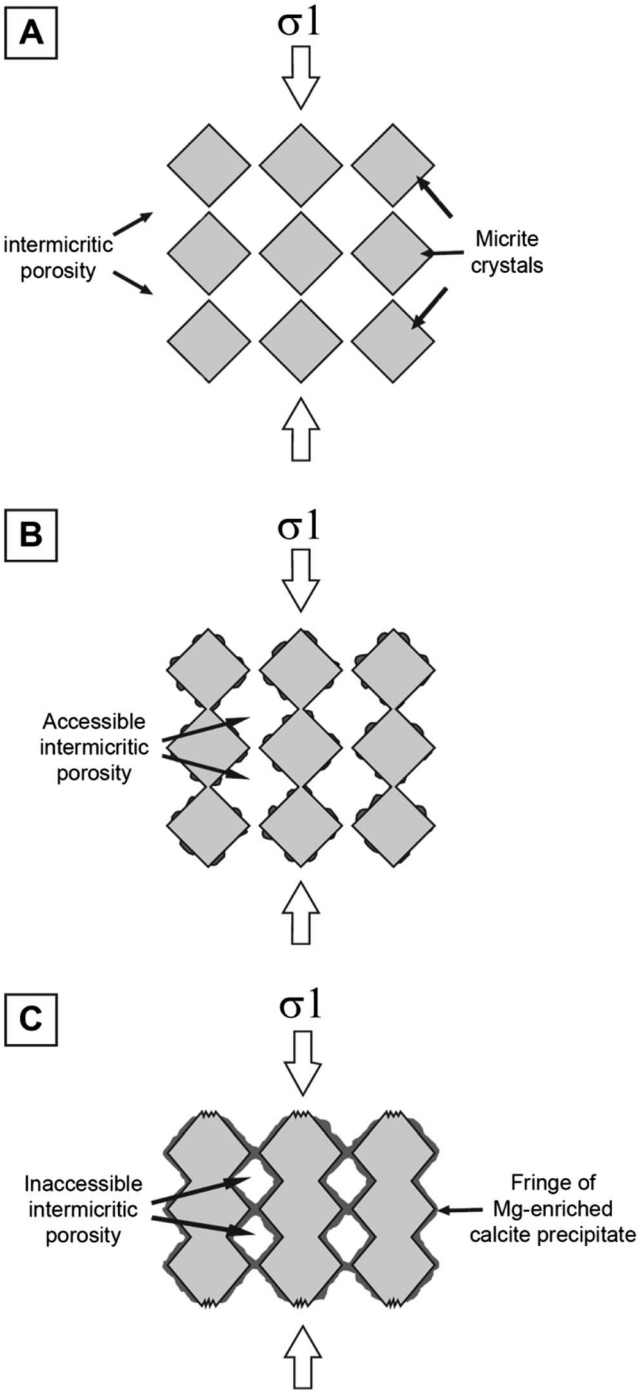

Figure 17. Schematic view of the effect of the pressure dissolution process on microporosity. (a) Initial state. (b) After Experiment I. (c) After Experiments II and III.

conditions. In addition, this experimental setup is not limited to the study of carbonate diagenesis; it can also be applied to the study of siliciclastic diagenesis or other consolidated rocks.

This setup has a fluid circulation system that can be used to investigate the impact of pore fluid composition during burial diagenesis. Actually, several studies have already evidenced the importance of fluid composition in the preservation of good reservoir properties. For example, the effects of phosphate [*Jonasson et al*., 1996; *Zhang and Spiers*, 2005a, 2005b; *Walter and Hanor*, 1979; *Dekanel and Morse*, 1978; *Katsifaras and Spanos*, 1999; *Alkattan et al*., 2002; *Plant and House*, 2002; *Dove and Hochella*, 1993], magnesium [*Zhang and Spiers*, 2005a; *Davis et al*., 2000], and salinity [*De Meer and Spiers*, 1999; *Liteanu and Spiers*, 2009], all of which are known to be inhibitors of calcite dissolution and therefore pressure solution, have already been investigated. In addition, hydrocarbons can also be injected in the tested sample, thus allowing for the simulation of early or late hydrocarbon injection in a reservoir. Therefore, we could investigate the effects of petroleum emplacement and its timing during diagenesis, which may play a major role in the preservation of porosity [*Neilson et al*., 1998; *Worden et al*., 1998; *Heasley et al*., 2000; *Neilson and Oxtoby*, 2008]. Experimental study on how these parameters influence consolidated rocks under high pressure/stresses and temperature is of great interest and should help to better understand the preservation of desirable reservoir properties at great depth.

5. Conclusions

A new experimental device, allowing both the experimental simulation of DBRs (deeply buried reservoirs) pressure/stresses/temperature conditions (80°C, 60 MPa of confining pressure, and differential stress up to 40 MPa) and the circulation of different fluids, was developed to study the chemomechanical behavior of rock samples. We followed a new multidisciplinary approach, which cover a wide field of scientific domains including mechanics, petrophysics, chemistry, and petrology, for the purpose of this study. We tested mechanically (four triaxial multistep creep tests) core samples of an early cemented bioclastic limestone, and we analyzed creep deformations, chemistry of pore fluids, and petrographical and petrophysical properties of samples.

We tested fluids with different flow conditions (no flow and flow through) and chemical compositions (natural meteoric water with and without phosphate ions).

Our experimental results showed that porosity reduction of a carbonate rock during deep burial is mainly due to a coupled chemomechanical process named PSC (pressure solution creep) which is inhibited in the presence of phosphate ions in the pore fluid. Actually, the precipitation of a fringe of calcite on free pore walls of micrites blocks the microporosity between micrite crystals, thus rendering the microporosity inaccessible to the high-pressure mercury (and probably to any fluid). Hence, the total connected porosity measured with mercury intrusion porosimetry decreased strongly (microporosity is not visible anymore in the porous spectrum), whereas the total porosity (determined with helium pycnometer) did not change significantly after experimentation. The preservation of macropores, which were not affected by the PSC process, allows the preservation of permeability. In addition, calcite solubility is positively dependent on mechanical parameters (axial compaction and applied axial stress). This relationship suggests that calcite can precipitate during decompression of deep basinal fluids, resulting in changes in porosity. A comparison of experimental results with theoretical calculations showed that a better understanding of the PSC process and the integration of the PSC process into calculation databases would greatly improve the modeling of DBR.

This present study provides therefore a new understanding of the behavior of reservoir rocks in deep burial conditions that could not be provided through investigations using classical laboratory tests. The experimental setup and protocol developed for the purpose of this study provide a background for experimental investigations of parameters involved in burial.

Acknowledgments

This research was supported by Total. We would like to thank O. Chailan, E. Gaucher, J.P. Girard, and T. Rossi for their scientific advice. The setup was conceived and assembled at the GeoRessources Laboratory, and we would like to thank all of the members of the "Hydrogeomeca multi-scale" team (P. Gaire, L. Schoumaker, M. Moumni, and M. Pierson). We are also grateful for the LA-ICP-MS team (M.C. Boiron, P. Lach, and M. Leisen). The MEB technical expertise of L. Mouton and S. Mathieu (SCMEM Nancy) is also gratefully acknowledged and the ionic chromatography expertise of C. Despas (LEM laboratory).

References

Alkattan, M., E. H. Oelkers, J. L. Dandurand, and J. Schott (2002), An experimental study of calcite dissolution rates at acidic conditions and 25°C in the presence of $NaPO_3$ and $MgCl_2$, *Chem. Geol.*, *190*, 291–302.

Atkinson, B. K. (1984), Subcritical crack growth in geological materials, *J. Geophys. Res.*, *89*, 4077–4114.

Atkinson, B. K., and P. G. Meredith (1987), The theory of subcritical crack growth with applications to minerals and rocks, in *Fracture Mechanics of Rock*, edited by B. K. Atkinson, pp. 111–166, Academic Press, London, U. K.

Baud, P., A. Schubnel, and T.-F. Wong (2000), Dilatancy, compaction, and failure mode in Solnhofen limestone, *J. Geophys. Res.*, *105*, 19,289–19,303.

Baud, P., S. Vinciguerra, C. David, A. Cavallo, E. Walker, and T. Reuschlé (2009), Compaction and failure in high porosity carbonates: Mechanical data and microstructural observations, *Pure Appl. Geophys.*, *166*, 869–898.

Bell, J. S., and G. Caillet (1994), A reinterpretation of the stress regime of the Aquitaine basin, southwestern France, and implications for hydrocarbon recovery, in *Hydrocarbon and Petroleum Geology of France*, Special Publication of the European Association of Petroleum Geoscientists, vol. 4, edited by A. Mascle, pp. 209–219, Springer-Verlag Berlin and Heidelberg GmbH & Co. K. Berlin, Germany.

Bieniawski, Z. T. (1967), Mechanism of brittle fracture of rock, parts I, II and III, *Int. J. Rock Mech. Min. Sci. Geomech. Abstr.*, *4*, 395–430.

Binh, N. T. T., T. Tokunaga, H. P. Son, and M. V. Binh (2007), Present-day stress and pore pressure fields in the Cuu Long and Nam Con Son Basins, offshore Vietnam, *Mar. Pet. Geol.*, *24*, 607–615.

Bjørlykke, K., and K. Høeg (1997), Effects of burial diagenesis on stresses, compaction and fluid flow in sedimentary basins, *Mar. Pet. Geol.*, *14*(3), 267–276.

Brantut, N., M. J. Heap, P. G. Meredith, and P. Baud (2013), Time-dependent cracking and brittle creep in crustal rocks: A review, *J. Struct. Geol.*, *52*, 17–43.

Caciagli, N. C., and C. E. Manning (2003), The solubility of calcite in water at 6–16 kbar and 500–800°C, *Contrib. Mineral. Petrol.*, *146*, 275–285.

Coelho, L. C., A. C. Soares, N. F. F. Ebecken, J. L. Drummond Alves, and L. Landau (2006), Modelling mechanical behaviour of limestone under reservoir conditions, *Int. J. Numer. Anal. Methods Geomech.*, *30*, 1477–1500.

Croizé, D., F. Renard, K. Bjørlykke, and D. K. Dysthe (2010a), Experimental calcite dissolution under stress: Evolution of grain contact microstructure during pressure solution creep, *J. Geophys. Res.*, *115*, B09207, doi:10.1029/2010JB000869.

Croizé, D., S. N. Ehrenberg, K. Bjørlykke, F. Renard, and J. Jahren (2010b), Petrophysical properties of bioclastic platform carbonates: Implications for porosity controls during burial, *Mar. Pet. Geol.*, *27*(8), 1765–1774.

Croizé, D., F. Renard, and J.-P. Gratier (2013), Compaction and porosity reduction in carbonates: A review of observations, theory, and experiments, in *Advances in Geophysics*, chap. 3, vol. 54, edited by R. Dmowska, pp. 181–238, Elsevier.

Dautriat, J., N. Gland, A. Dimanov, and J. Raphanel (2011), Hydromechanical behavior of heterogeneous carbonate rock under proportional triaxial loadings, *J. Geophys. Res.*, *116*, B01205, doi:10.1029/2009JB000830.

Davis, K. J., P. M. Dove, and J. J. Yoreo (2000), The role of Mg^{2+} as an impurity in calcite growth, *Science*, *290*, 1134–1137.

De Meer, S., and C. J. Spiers (1999), Influence of pore-fluid salinity on pressure solution creep in gypsum, *Tectonophysics*, *308*, 311–330.

De Meer, S., C. J. Spiers, C. J. Peach, and T. Watanabe (2002), Diffusive properties of fluid-filled grain boundaries measured electrically during active pressure solution, *Earth Planet. Sci. Lett.*, *200*, 147–157.

Dekanel, J., and J. W. Morse (1978), The chemistry of orthophosphate uptake from seawater on to calcite and aragonite, *Geochim. Cosmochim. Acta*, *42*, 1335–1340.

Deville de Periere, M., C. Durlet, E. Vennin, L. Lambert, R. Bourillot, B. Caline, and E. Poli (2011), Morphometry of micrites particles in cretaceous microporous limestones of the Middle East: Influence on reservoir properties, *Mar. Pet. Geol.*, *28*, 1727–1750.

Dove, P. M., and M. F. Hochella (1993), Calcite precipitation mechanisms and inhibition by orthophosphate: In situ observations by scanning force microscopy, *Geochim. Cosmochim. Acta*, *57*, 705–714.

Duan, Z., and D. Li (2008), Coupled phase and aqueous species equilibrium of the H2O-CO2-CaCO3 system from 0 to 250°C, 1 to 1000 bar with NaCl concentrations up to saturation of halite, *Geochim. Cosmochim. Acta*, *72*, 5128–5145.

Dysthe, D. K., F. Renard, J. Feder, B. Jamtveit, P. Meakin, and T. Jossang (2003), High-resolution measurements of pressure solution creep, *Phys. Rev. E*, *68*, Article 011603.
Dysthe, D. K., R. A. Wogelius, C. C. Tang, and A. A. Nield (2006), Evolution of mineral-fluid interfaces studied at pressure with synchrotron X-ray techniques, *Chem. Geol.*, *230*, 232–241.
Ehrenberg, S. N., and P. H. Nadeau (2005), Sandstone vs. carbonate petroleum reservoirs; A global perspective on porosity-depth and porosity-permeability relationships, *AAPG Bull.*, *89*(4), 435–445.
Elliott, G. M., and E. T. Brown (1985), Yield of a soft, high porosity rock, *Geotechnique*, *35*(4), 413–423.
Friedman, G., S. A. Reeckmann, and B. Borak (1981), Carbonate deformation mechanisms in the world's deepest wells (nearly equal 9 km), *Tectonophysics*, *74*(3–4), T15–T19.
Gratier, J. P. (1993), Experimental pressure solution of halite by an indenter technique, *Geophys. Res. Lett.*, *20*, 1647–1650.
Gunzburger, Y. (2010), Stress state interpretation in light of pressure-solution creep: Numerical modelling of limestone in the Eastern Paris Basin, France, *Tectonophysics*, *483*, 377–389.
Heasley, E. C., R. H. Worden, and J. P. Hendry (2000), Cement distribution in a carbonate reservoir: Recognition of a palaeo oil-water contact and its relationship to reservoir quality in the Humbley Grove field, Onshore, UK, *Mar. Pet. Geol.*, *17*, 639–654.
Holbrook, P. (1999), A simple closed form force balanced solution for pore pressure overburden and the principal stresses in the Earth, *Mar. Pet. Geol.*, *16*, 303–319.
Johnson, J., G. Anderson, and D. Parkhurst (2000), Database 'thermo.com.v8.r6.230'. Rev. 1.11, Lawrence Livermore Natl. Lab., Livermore, California.
Jonasson, R. G., K. Rispler, B. Wiwchar, and W. D. Gunter (1996), Effect of phosphonate inhibitors on calcite nucleation kinetics as a function of temperature using light scattering in an autoclave, *Chem. Geol.*, *132*, 215–225.
Katsifaras, A., and N. Spanos (1999), Effect of inorganic phosphate ions on the spontaneous precipitation of vaterite and on the transformation of vaterite to calcite, *J. Cryst. Growth*, *204*, 183–190.
Konstantinovskaya, E., M. Malo, and D. A. Castillo (2012), Present-day stress analysis of the St Lawrence Lowlands sedimentary basin (Canada) and its implications for caprock integrity during CO_2 injection operations, *Tectonophysics*, *518–521*, 119–137.
Lehner, F. K. (1995), A model for intergranular pressure solution in open systems, *Tectonophysics*, *245*, 153–170.
Leisen, M., J. Dubessy, M. C. Boiron, and P. Lach (2012a), Improvement of the determination of element concentrations in quartz-hosted fluid inclusions by LA-ICP-MS and Pitzer thermodynamic modeling of ice melting temperature, *Geochim. Cosmochim. Acta*, *90*, 110–125.
Leisen, M., M. C. Boiron, A. Richard, and J. Dubessy (2012b), Determination of Cl and Br concentrations in individual fluid inclusions by combining microthermometry and LA-ICPMS analysis: Implications for the origin of salinity in crustal fluids, *Chem. Geol.*, *330–331*, 197–206.
Leythaeuser, D., O. Borromeo, F. Mosca, R. di Primio, M. Radke, and R. G. Schaefer (1995), Pressure solution in carbonate source rocks and its control on petroleum generation and migration, *Mar. Pet. Geol.*, *12*, 717–733.
Liteanu, E., and C. J. Spiers (2009), Influence of pore fluid salt content on compaction creep of calcite aggregates in the presence of supercitical CO_2, *Chem. Geol.*, *265*, 134–147.
Lockner, D. (1993), Room temperature creep in saturated granite, *J. Geophys. Res.*, *98*, 475–487.
Marini, L. (2007), *Geological Sequestration of Carbon Dioxide: Thermodynamics, Kinetics, and Reaction Path Modeling*, vol. 11, 1st ed., pp. 453, Elsevier.
Meyer, H. J. (1984), The influence of impurities on the growth rate of calcite, *J. Cryst. Growth*, *66*, 639–646.
Neilson, J. E., and N. H. Oxtoby (2008), The relationship between petroleum, exotic cements and reservoir quality in carbonates—A review, *Mar. Pet. Geol.*, *25*, 778–790.
Neilson, J. E., N. H. Oxtoby, M. D. Simmons, I. R. Simpson, and N. A. Fortunatova (1998), The relationship between petroleum emplacement and carbonate reservoir quality: Examples from Abu Dhabi and the Amu Darya Basin, *Mar. Pet. Geol.*, *15*, 57–72.
Parkhurst, D. L., and C. A. J. Appelo (1999), *User's Guide to PHREEQC (Version 2). A Computer Program for Speciation, Batch-Reaction, One Dimensional Transport, and Inverse Geochemical Calculations*, Water-resources investigations report, vol. 99, edited by USGS, Denver, Colo, USA.
Paterson, M. S. (1973), Nonhydrostatic thermodynamics and its geologic applications, *Rev. Geophys. Space Phys.*, *11*, 355–389.
Paterson, M. S., and T.-F. Wong (2005), *Experimental Rock Deformation—The Brittle Field*, 2nd ed., 347 pp., Springer-Verlag, Berlin, Germany.
Plant, L. J., and W. A. House (2002), Precipitation of calcite in the presence of inorganic phosphates, *Colloids Surf. A*, *203*, 43–153.
Plummer, L. N., and T. M. L. Wigley (1976), The dissolution of calcite in CO_2-saturated solutions at 25°C and 1 atmosphere total pressure, *Geochim. Cosmochim. Acta*, *40*, 191–202.
Plummer, L. N., T. M. L. Wigley, and D. L. Parkhurst (1978), The kinetics of calcite dissolution in CO_2-water systems at 5° and 60°C and 0.0 to 1.0 atm CO_2, *Am. J. Sci.*, *278*, 179–216.
Pokrosky, O. S., S. V. Golubev, and J. Schott (2005), Dissolution kinetics of calcite, dolomite and magnesite at 25°C and 0 to 50 atm pCO_2, *Chem. Geol.*, *217*, 239–255.
Pokrosky, O. S., S. V. Golubev, J. Schot, and A. Castillo (2009), Calcite, dolomite and magnesite dissolution kinetics in aqueous solutions at acid to circumneutral pH, 25 to 150°C and 1 to 55 atm pCO_2: New constraints on CO_2 sequestration in sedimentary basins, *Chem. Geol.*, *265*, 20–32.
Price, R. M., M. Reza Savabi, J. L. Jolicoeur, and S. Roy (2010), Adsorption and desorption of phosphate on limestone in experiments simulating seawater intrusion, *Appl. Geochem.*, *25*, 1085–1091.
Reddy, M. M. (1977), Crystallization of calcium carbonate in the presence of trace concentrations of phosphorus-containing anions. I. Inhibition by phosphate and glycerophosphate ions at pH 8.8 and 25°C, *J. Cryst. Growth*, *41*, 287–295.
Røyne, A., J. Bisschop, and D. K. Dysthe (2011), Experimental investigation of surface energy and subcritical crack growth in calcite, *J. Geophys. Res.*, *116*, B04204, doi:10.1029/2010JB008033.
Rutter, E. H. (1974), The influence of temperature, strain rate and interstitial water in the experimental deformation of calcite rocks, *Tectonophysics*, *22*, 311–334.
Rutter, E. H. (1976), The kinetics of rock deformation by pressure solution, *Philos. Trans. R. Soc. Lond.*, *283*, 203–219.
Rutter, E. H. (1983), Pressure solution in nature, theory and experiment, *J. Geol. Soc. London*, *140*, 725–740.
Schmoker, J. W. (1984), Empirical relation between carbonate porosity and thermal maturity—An approach to regional porosity prediction, *AAPG Bull.*, *68*, 1697–1703.
Schmoker, J. W., and R. B. Halley (1982), Carbonate porosity versus depth: A predictable relation for South Florida, *AAPG Bull.*, *66*, 2561–2570.
Scholz, C. H. (1968), Mechanism of creep in brittle rock, *J. Geophys. Res.*, *73*, 3295–3302.
Schubnel, A., J. Fortin, L. Burlini, and Y. Gueguen (2005), Damage and recovery of calcite rocks deformed in the cataclastic regime, *Geol. Soc. Spec. Publ.*, *245*, 203–221.
Sorby, H. C. (1863), On the direct correlation of mechanical and chemical forces, *Proc. R. Soc. London*, *12*, 1862–1863.

Spiers, C. J., P. M. T. M. Schutjens, R. H. Brzesowsky, C. J. Peach, J. L. Liezenberg, and H. J. Zwart (1990), Experimental determination of constitutive parameters governing creep of rocksalt by pressure solution, in *Deformation Mechanism, Rheology and Tectonics*, Special Publications, vol. 54, edited by R. J. Knipe and E. H. Rutter, pp. 215–227, Geological Society, London, U. K.

Tada, R., and R. Siever (1989), Pressure solution during diagenesis, *Annu. Rev. Earth Planet. Sci.*, *17*, 89–118.

Tada, R., R. Maliva, and R. Siever (1987), A new mechanism for pressure solution in porous quartzose sandstone, *Geochim. Cosmochim. Acta*, *51*, 2295–2301.

Vajdova, V., P. Baud, and T. Wong (2004), Compaction, dilatancy, and failure in porous carbonate rocks, *J. Geophys. Res.*, *109*, B05204, doi:10.1029/2003JB002508.

Vajdova, V., W. Zhu, T.-M. Natalie Chen, and T.-F. Wong (2010), Micromechanics of brittle faulting and cataclastic flow in Tavel limestone, *J. Struct. Geol.*, *32*, 1158–1169.

Vajdova, V., P. Baud, L. Wu, and T.-F. Wong (2012), Micromechanics of inelastic compaction in two allochemical limestones, *J. Struct. Geol.*, *43*, 100–117.

Van Noort, R., H. J. M. Visser, and C. J. Spiers (2008), Influence of grain boundary structure on dissolution controlled pressure solution and retarding effects of grain boundary healing, *J. Geophys. Res.*, *113*, B03201, doi:10.1029/2007JB005223.

Walter, L. M., and J. S. Hanor (1979), Effect of orthophosphate on the dissolution kinetics of biogenic magnesian calcites, *Geochim. Cosmochim. Acta*, *43*, 1377–1385.

Weyl, P. K. (1959), Pressure solution and the force of crystallization—A phenomenological theory, *J. Geophys. Res.*, *69*, 2001–2025.

Wong, T.-F., and P. Baud (2012), The brittle-ductile transition in porous rock: A review, *J. Struct. Geol.*, *44*, 25–53.

Worden, R. H., N. H. Oxtoby, and P. C. Smalley (1998), Can oil emplacement prevent quartz cementation in sandstones?, *Pet. Geosci.*, *4*, 129–137.

Xie, S. Y., J. F. Shao, and W. Y. Xu (2011), Influences of chemical degradation on mechanical behaviour of a limestone, *Int. J. Rock Mech. Min. Sci.*, *48*, 741–747.

Yasuhara, H., D. Elsworth, and A. Polak (2003), A mechanistic model for compaction of granular aggregates moderated by pressure solution, *J. Geophys. Res.*, *108*(B11), 2530, doi:10.1029/2003JB002536.

Zhang, X., and C. J. Spiers (2005a), Compaction of granular calcite by pressure solution at room temperature and effects of pore fluid chemistry, *Int. J. Rock Mech. Min. Sci.*, *42*, 950–960.

Zhang, X., and C. J. Spiers (2005b), Effects of phosphate ions on intergranular pressure solution in calcite: An experimental study, *Geochim. Cosmochim. Acta*, *69*, 5681–5691.

Zhu, W., P. Baud, and T.-F. Wong (2010), Micromechanics of cataclastic pore collapse in limestone, *J. Geophys. Res.*, *115*, B04405, doi:10.1029/2009JB006610.

Zubtsov, S., F. Renard, J. P. Gratier, R. Guiguet, D. K. Dysthe, and V. Traskine (2004), Experimental pressure solution compaction of synthetic halite/calcite aggregates, *Tectonophysics*, *385*, 45–57.